PTP-MEG2 regulates quantal size and fusion pore opening through two distinct structural bases and substrates

Yun-Fei Xu*[#1], Xu Chen[#2], Zhao Yang[1], Peng Xiao[1], Chun-Hua Liu[3], Kang-Shuai Li[1], Xiao-Zhen Yang[4], Yi-Jing Wang[1], Qi Liu[2], Sheng Zhang[7], Chuan Wang[5], Yue-Mao Shen[6], Zhong-Yin Zhang[#7], Wei-Dong Zhao[8], Chang-He Wang[9], Zhi-Liang Ji[4], Min Cui*[2], Jin-Peng Sun*[1] and Xiao Yu*[&2]

Affiliations:

[1]Key Laboratory Experimental Teratology of the Ministry of Education and Department of Biochemistry and Molecular Biology, Shandong University School of Medicine, 44 Wenhua Xi Road, Jinan, Shandong, 250012, China

[2]Key Laboratory Experimental Teratology of the Ministry of Education and Department of Physiology, Shandong University School of Medicine, 44 Wenhua Xi Road, Jinan, Shandong, 250012, China

[3]Department of Physiology, Taishan Medical University, Taian, Shandong 271000, China.

[4]State Key Laboratory of Cellular Stress Biology, School of Life Sciences, Xiamen University, Xiamen 361102, Fujian, China

[5]Department of Pharmacology, Hebei Medical University, Shijiazhuang, China

[6]Key Laboratory of Chemical Biology (Ministry of Education), School of Pharmaceutical Sciences, Shandong University, Jinan, Shandong 250012, China

[7]Departments of Medicinal Chemistry and Molecular Pharmacology and of Chemistry, Purdue Center for Cancer Research, and Purdue Center for Drug Discovery, Purdue University, 575 Stadium Mall Drive, West Lafayette, IN 47907, USA.

[8]Department of Developmental Cell Biology, China Medical University, 77 Puhe Road, Shenbei New District, 110122 Shenyang, China.

[9]Center for Mitochondrial Biology and Medicine, The Key Laboratory of Biomedical Information Engineering of Ministry of Education, School of Life Science and Technology, Xi'an Jiaotong University, Xi'an, China

[#] These authors contributed equally to this work

[&]Lead author

* Corresponding author: Jin-Peng Sun (corresponding author)
E-mail: sunjinpeng@bjmu.edu.cn
Xiao Yu (corresponding author)
E-mail: yuxiao@sdu.edu.cn
Min Cui (corresponding author)
E-mail: cuimin@sdu.edu.cn
Yun-Fei Xu (corresponding author)
E-mail:xuyunfei1988@126.com

SUMMARY

The tyrosine phosphorylation of secretion machinery proteins is a crucial regulatory mechanism for exocytosis. However, the participation of tyrosine phosphatases in different exocytosis stages has not been defined. Here, we demonstrated that PTP-MEG2 controls multiple steps of catecholamine secretion. Biochemical and crystallographic analysis revealed key residues that govern the PTP-MEG2 and NSF-pY^{83} site interactions, specify PTP-MEG2 substrate selectivity and modulate the fusion of catecholamine-containing vesicles. Unexpectedly, delineation of the PTP-MEG2 mutants along with the NSF interface revealed that PTP-MEG2 controls the fusion pore opening through another unknown substrate. Utilizing a bioinformatics search and biochemical and electrochemical screening, we uncovered that PTP-MEG2 regulates the opening and extension of the fusion pore by dephosphorylating the MUNC18-1 Y^{145} site, which is associated with epileptic encephalopathy. The crystal structure of the PTP-MEG2/phospho-MUNC18-1-pY^{145} segment confirmed the interaction of PTP-MEG2 with MUNC18-1 through a distinct structural basis. Our studies extended mechanism insights in complex exocytosis processes.

KEY WORDS:

exocytosis, tyrosine phosphorylation, structure, catecholamine, PTP-MEG2

HIGHLIGHTS:

PTP-MEG2 regulates multiple steps of exocytosis.
A crystal structure of the PTP-MEG2/phosphor-NSF-pY^{83} segment was obtained.
Functional delineation of the PTP-MEG2/NSF interface resulted in uncovering unknown PTP-MEG2 substrates.
PTP-MEG2 regulates fusion pore opening and extension through the MUNC18-1 pY^{145} site.
The distinct structural bases of the recognition of substrates by PTP-MEG2 allows selective inhibitor design.

INTRODUCTION

Secretion via vesicle exocytosis is a fundamental biological event involved in almost all

physiological processes (Wu et al., 2014, Dittman and Ryan, 2019, Neher and Brose, 2018). The contents of secreted vesicles include neuronal transmitters, immune factors and other hormones (Alvarez de Toledo et al., 1993, Sudhof, 2013, Magadmi et al., 2019). There are three main exocytosis pathways in secretory cells, namely, full-collapse fusion, kiss-and-run, and compound exocytosis, which possess different secretion rates and lease amount (Sudhof, 2004). It was previously reported that the phosphorylation of critical proteins at serine/threonine or tyrosine residues participated in stimulus–secretion coupling in certain important exocytosis processes, for example, the secretion of insulin from pancreatic β cells and of catecholamine from the adrenal medulla (Ortsater et al., 2014, Seino et al., 2009, Laidlaw et al., 2017). However, the exact roles of protein tyrosine phosphatases (PTPs) in the regulation of key hormone secretion procedures are not fully understood.

The 68-kDa PTP-MEG2, encoded by *ptpn9*, is a non-receptor classical PTP encompassing a unique N-terminal domain with homology to the human CRAL/TRIO domain and yeast Sec14p (Alonso et al., 2004, Gu et al., 1992, Zhang et al., 2012, Zhang et al., 2016, Cho et al., 2006, Huynh et al., 2004). The N-terminal Sec14p homology domain of PTP-MEG2 recognizes specific phospholipids in the membrane structure and is responsible for its specific subcellular location. In secretory immune cells, PTP-MEG2 has been suggested to regulate vesicle fusion via directly dephosphorylating the pY^{83} site of N-ethylmaleimide-sensitive fusion protein (NSF) (Huynh et al., 2004). However, many key issues regarding PTP-MEG2-regulated cell secretion remain controversial or even unexplored. For example, it is uncertain whether PTP-MEG2 regulates vesicle exocytosis only inside immune cells (Zhang et al., 2016) and play only insignificant roles in other hormone secretion processes. It remains elusive whether PTP-MEG2 regulates vesicle trafficking pathways other than NSF-mediated vesicle fusion.

Functional characterization of PTP-MEG2 in vivo normally requires a knockout model; however, PTP-MEG2-deficient mice show neural tube and vascular defects, and the deficiency is embryonic lethal (Wang et al., 2005). Alternatively, a specific inhibitor of PTP has the properties of fast action and no compensatory effect, which enable it to serve as a powerful tool to investigate PTP-MEG2 functions (Zhang et al., 2012, Yu and Zhang, 2018). Recently, we developed a potent and selective PTP-MEG2 inhibitor, Compound 7, that has a Ki of 34 nM and shows at least 10-fold selectivity for PTP-MEG2 over more than 20 other PTPs (Zhang et al., 2012). The application of this selective PTP-MEG2 inhibitor in combination with electrochemical approaches enabled us to reveal that PTP-MEG2 regulates multiple steps of catecholamine secretion from the adrenal medulla by controlling the vesicle size, the release probabilities of individual vesicles and the initial opening of the fusion pore during exocytosis. Further crystallographic study of the PTP-MEG2 protein in complex with the pY^{83}-NSF fragment and enzymological kinetic studies captured the transient interaction between PTP-MEG2 and NSF and provided the structural basis for PTP-MEG2 substrate specificity.

Interestingly, by delineating the substrate specificity of deficient PTP-MEG2 mutants in the study of catecholamine secretion from primary chromaffin cells, our results suggested that PTP-MEG2 regulated the initial opening of the fusion pore during exocytosis by regulating substrates other than the known NSF through distinct structural bases. We therefore took advantage of this key knowledge and utilized bioinformatics analysis, GST pull-down screening, enzymology and electrochemical to identify the potential key PTP-MEG2 substrates involved in fusion pore opening. These experiments led to the identification of several new PTP-MEG2 substrates in the adrenal medulla, of which MUNC18-1-Y^{145} is the crucial dephosphorylation site of PTP-MEG2 in the regulation of initial pore opening and expansion. Further crystallographic analysis and functional assays with MUNC18-1 Y^{145} revealed the structural basis of the recognition of MUNC18-1 by PTP-MEG2 and how Y^{145} phosphorylation regulates fusion pore opening. Our results provide new information and mechanistic insights regarding how dynamic tyrosine phosphorylation and PTP-MEG2 explicitly regulate different processes of vesicle fusion and hormone secretion, both of which may lead to human disease when dysregulated.

RESULTS

Phosphatase activity of PTP-MEG2 is required for catecholamine secretion from adrenal glands

Endogenous PTP-MEG2 expression was readily detected in mouse adrenal gland and chromaffin cell line PC12 cells (Supplemental Fig. 1-1A-B). PTP-MEG2 knockout is embryonic lethal (Wang et al., 2005). To investigate the functional role of PTP-MEG2 in catecholamine secretion from adrenal glands, we therefore applied our newly developed specific PTP-MEG2 inhibitor (Compound 7) (Supplemental Fig. 1-1C). The inhibitor Compound 7 is a potent PTP-MEG2 inhibitor, with a potency of 34 nM and extraordinary selectivity against other phosphatases (Zhang et al., 2012). The administration of either high concentrations of potassium chloride (70 mM) or 100 nM Angiotensin II (AngII) significantly increased the secretion of both epinephrine (EPI) and norepinephrine (NE) from adrenal medulla, as previously reported (Liu et al., 2017, Teschemacher and Seward, 2000), and this effect was specifically blocked by pre-incubation with Compound 7 (2 μM) for 1 hour (Fig. 1A-D). Notably, basal catecholamine secretion was also decreased after pre-incubation with Compound 7 (Fig. 1A-D). However, the catecholamine contents were not changed in response to Compound 7 incubation (Supplemental Fig. 1-1D-E). These results indicated that PTP-MEG2 plays an essential role in catecholamine secretion from the adrenal medulla.

PTP-MEG2 inhibition reduced the quantal size and the release probabilities of catecholamine secretion from individual vesicles.

We used the carbon fiber electrode (CFE) to characterize the effects of PTP-MEG2 inhibition on the kinetics of catecholamine secretion from primary cultured chromaffin cells (Chen et al., 2005, Harada et al., 2015) (Fig. 1E-F and Supplemental Fig. 1-1F-G). The Angiotensin II-induced catecholamine secretion was gradually attenuated by increasing the concentration of Compound 7 after pre-incubation with the primary chromaffin cells, from 20% at 100 nM Compound 7 to 80% at 2 μM inhibitor (Fig. 1E-F and Supplemental Fig. 1-1 F-H). We then compared isolated amperometric spikes of chromaffin cells pre-incubated with different concentrations of Compound 7 to determine the effect of the inhibition of PTP-MEG2 activity on quantal size (total amperometric spike charge) and vesicle release probability. The application of PTP-MEG2 inhibitor reduced quantal size, as indicated by statistical analysis of the quantal size distribution and averaged amperometric spike amplitude (Fig. 1G and Supplemental Fig. 1-1 I). Specifically, the peak of the amperometric spikes was reduced from 1.1 pC to 0.5 pC after incubation with 400 nM Compound 7 (Fig. 1G). The number of AngII-induced amperometric spikes was also significantly decreased in the presence of Compound 7, suggesting that either the release probabilities of individual vesicles or the size of the readily released pool was affected (Supplemental Fig. 1-1 J).

We next used transmission electron microscopy to examine the location of the large-dense-core vesicles (LDCVs) in the adrenal gland medulla after incubation with AngII and Compound 7 (Fig. 1H-M and Supplemental Fig. 1-2 A-B). There was no significant difference in the location of the LDCVs when these vesicles were sub-grouped by 200 nanometre bins according to their distance from the chromaffin plasma membrane (Fig. 1J). However, the application of 400 nM Compound 7 significantly decreased the number of docking vesicles in contact with the plasma membrane (Fig. 1K-L). These results indicated that the inhibition of PTP-MEG2 activity by Compound 7 decreased the release probabilities of individual vesicles but did not affect the size of the readily released pool. Moreover, the observed numbers of LDCVs with diameters larger than 150 nm observed by electron microscopy were significantly decreased by more than 70% after incubation with Compound 7 (Fig. 1M), which is consistent with the statistical analysis of the total amperometric spike charge obtained by electrochemical measurement (Supplemental Fig. 1-1H-M).

PTP-MEG2 regulates the initial opening of the fusion core

Generally, the presence of pre-spike foot (PSF) is a common phenomenon preceding large amperometric spikes of catecholamine secretion in chromaffin cells, while stand-alone foot (SAF) is considered to represent "kiss-and-run" exocytosis (Chen et al., 2005). Both PSF and SAF are generally considered indications of the initial opening of the fusion pore (Alvarez de Toledo et al., 1993, Zhou et al., 1996). In this study, the PSF frequency significantly decreased from 25% to 3% after pre-incubation with Compound 7 in response to AngII stimulation (Fig. 1N). The inhibitor Compound 7 had no significant effect on the PSF duration (Supplemental Fig. 1-2 C-D) but markedly reduced the amplitude and charge of PSF (Supplemental Fig. 1-2 E-F). Similar results were observed for the SAF (Supplemental Fig. 1-2 G-J). The PTP-MEG2 inhibitor Compound 7 reduced the SAF percentage from 18% to 4% (Fig. 1N). Intriguingly, the duration of SAF was also decreased with increasing Compound 7 concentration, in contrast to the PSF (Supplemental Fig. 1-2H). Additionally, the average amplitude and charge of SAF decreased from 14 pA to 5 pA and from 150 fC to 65 fC, respectively (Supplemental Fig. 1-2 I-J). These results suggested that PTP-MEG2 activity was required for the initial opening of the fusion core but had no effect on the endocytosis rate of the partially fused vesicles.

The crystal structure of the PTP-MEG2/phospho-NSF complex revealed significant structural rearrangement in the WPD loop and β3-loop-β4

PTP-MEG2 is known to modulate interleukin-2 secretion in macrophages via de-phosphorylating NSF, a key regulator in vesicle fusion (Huynh et al., 2004). In response to stimulation with either high potassium chloride or AngII, the two stimulators for catecholamine secretion from the adrenal medulla, the tyrosine phosphorylation of NSF increased, indicating that NSF phosphorylation actively participates in catecholamine secretion (Fig. 2A and Supplemental Fig. 2A-B). Moreover, a significant portion of NSF co-localized with PTP-MEG2 in adrenal medulla with AngII stimulation, and the trapping mutant PTP-MEG2-$C^{515}SD^{470}A$ interacted with the tyrosine-phosphorylated NSF from the adrenal medulla treated with peroxide (Fig. 2B-D and Supplemental Fig. 2C-D), indicating that PTP-MEG2 regulates catecholamine secretion in chromaffin cells through directly dephosphorylation of NSF.

We therefore co-crystallized PTP-MEG2/phospho-NSF-E^{79}-pY^{83}-K^{87}, and the structure was solved at 1.7 Å (Table 1). The 2Fo-Fc electron density map allowed unambiguous assignment of the phospho-NSF-E^{79}-pY^{83}-K^{87} in the crystal structure (Fig. 2E-F). Importantly, the binding of phospho-NSF-E^{79}-pY^{83}-K^{87} induced substantial conformational changes at both the WPD loop and β3-loop-β4 compared to the crystal structure of PTP-MEG2 alone (Barr et al., 2009) (Fig. 2G-H). Specifically, the interaction of the phosphate of the pY^{83} of the NSF

with the guanine group of the R^{521} of the PTP-MEG2 induced a rotation of approximately 90 degrees, which resulted in the movement of the W^{468} and a traverse of 7 Å of the WPD loop for a closed state (Fig. 2I-J). Unique to the PTP-MEG2/substrate complex, the movement of L^{466} in the WPD loop by 1.7 Å enabled the formation of a new hydrogen bond between its main chain carbonyl group and the side chain of R^{403} (Fig. 2I-J). The disruption of the salt bridge between E^{406} and R^{521} also contributed to the new conformational state of the N-terminal of β3-loop-β4 (Fig. 2K-L). The presence of phosphate in the PTP-MEG2 active site C-terminal to β3-loop-β4 caused a 180 degree rotation of the side chain of S^{516}, allowing its side chain oxygen to form a new hydrogen bond with the main chain carbonyl of the K^{411} (Fig. 2K-L). This structural rearrangement altered the side chain conformation of K^{411}, which pointed to the solvent region and formed new polar interactions with E^{406} and the carbonyl group of R^{409} (Fig. 2K-L). Moreover, the presence of the phospho-NSF-E^{79}-pY^{83}-K^{87} peptide between R^{409} and D^{335} disrupted their charge interaction, which enabled a movement of the main chain from G^{408} to K^{411}, accompanied by a side chain movement of R^{410} and the formation of new polar interactions with the main chain of P^{378} and C^{412} (Fig. 2M-N). The structural rearrangements that occurred at WPD and β3-loop-β4 enabled the accommodation of the phospho-substrate of PTP-MEG2 and may be important for its appropriate interaction with its physiological substrates/partners and subsequent activation.

Structural basis of the PTP-MEG2-NSF interaction

The structural analysis identified critical residues for phospho-substrate recognition by PTP-MEG2 (Fig. 3A). Y^{333} forms extensive hydrophobic interaction with the phenyl ring of the pY^{83} of NSF. Mutation of this residue caused a significant decrease of more than 3-fold in activity for both pNPP and phospho-NSF-peptide, suggesting that this residue is important for PTP-MEG2 recognition of all substrates with phenyl rings. N-terminal to pY^{83}, the side chain oxygen of S^{81} forms a hydrogen bond with the carbonyl oxygen of the main chain of R^{332} of PTP-MEG2. The carbonyl oxygen of the main chain of S^{81} forms a hydrogen bond with the amide of G^{334}, and L^{82} forms hydrophobic interactions with the side chain of D^{335} (Fig. 3A). Specifically, mutation of G^{334} to R impaired the activity of PTP-MEG2 towards the NSF-pY^{83} phospho-peptide but had no effect on its intrinsic pNPP activity, suggesting that G^{334} plays an important role in the recognition of the N-terminal conformation of the peptide substrate (Fig. 3B-C and Supplemental Fig. 3A-B).

The D^{335} in the pY binding loop of PTP-MEG2 is also critical for determining the peptide orientation of the substrate by forming important hydrogen bonds with the main chain amide

and carbonyl groups of pY^{83} and T^{84}. C-terminal to NSF-pY^{83}, Q^{559} forms a van der Waals interaction with T^{84}, and F^{85} forms substantial hydrophobic interactions with V^{336}, F^{556} and I^{519} (Fig. 3A). Accordingly, mutation of D^{335}A or Q^{559}A showed no significant effect on pNPP activity but substantially decreased their activities towards the phospho-NSF peptide (Fig. 3B-C and Supplemental Fig. 3A-B). Mutation of I^{519}A caused a decrease in the intrinsic activity of PTP-MEG2 and a further decrease of approximately 4-fold in its ability to dephosphorylate phospho-NSF-peptide. Moreover, Y^{471} forms extensive hydrophobic interactions with T^{84} and Y^{85} and a hydrogen bond with the carboxyl group of pY^{83}. Mutation of Y^{471} to either A or F greatly reduced its activity towards phospho-NSF- E^{79}-pY^{83}-K^{87} peptide but had little effect on pNPP dephosphorylation. Taken together, the structural analysis and enzymology studies identified G^{334}, D^{335}, Y^{471}, I^{519} and Q^{559} as critical residues for the substrate recognition of NSF by PTP-MEG2. Importantly, although none of these residues are unique to PTP-MEG2, the combination of these residues is not identical across the PTP superfamily but is conserved between PTP-MEG2 across different species, highlighting the important roles of these residues in mediating specific PTP-MEG2 functions (Fig. 3D and Supplemental Fig. 4).

Molecular determinants of Q559:D335 for the substrate specificity of PTP-MEG2

The pY+1 pocket is an important determinant of substrate specificity in different PTP superfamily members (Barr et al., 2009, Li et al., 2016, Yu et al., 2011, Wang et al., 2014). The pY+1 pocket of PTP-MEG2 was found to consist of D^{335}, V^{336}, F^{556} and Q^{559} (Fig. 4A). Unique to the PTP-MEG2/NSF-E^{79}-pY^{83}-K^{87} complex structure, a relatively small T^{84} residue occurs at the pY+1 position, in contrast to pY^{1163} in the PTP1B/EGFR-pY^{992} complex structure, D^{395} in the LYP/SKAP-HOM-pY^{75} complex structure and L^{1249} in the PTPN18/phospho-HER2-pY^{1248} complex structure (Fig. 4A). Although several PTPs have an equivalent D:Q pair similar to D^{335}:Q^{559} of PTP-MEG2 determining the entrance of the pY+1 residue into the pY+1 pocket, such as PTP1B, LYP, PTPN18, STEP, PTP-Meg1, SHP1, PTPH1 and SHP2, structural analysis indicated that the Cβ between Q^{559} and D^{335} is the smallest in PTP-MEG2, at least 1 Å narrower than in the other PTP structures examined (Fig. 4B). The narrower pY+1 pocket entrance could be a unique feature of the substrate recognition of PTP-MEG2.

PTP-MEG2 regulates two different processes of catecholamine secretion through a distinct structural basis

We next infected primary chromaffin cells with lentivirus encoding wild-type PTP-MEG2

or different mutants for electrochemical investigation of the structure-function relationship of PTP-MEG2 in the regulation of catecholamine secretion (Fig. 5A and Supplemental Fig. 5A-F). In addition to wild-type PTP-MEG2, we chose 5 PTP-MEG2 mutants, including $G^{334}R$, $D^{335}A$, $Y^{471}A$, $Y^{471}F$, $I^{519}A$ and $Q^{559}A$, whose positions are determinants of the interactions between PTP-MEG2 and NSF from the pY^{83}-1 position to the pY^{83}+2 position (Fig. 5B). The overexpression of wild-type PTP-MEG2 significantly increased both the number and amplitude of the amperometric spikes, which are indicators of the release probabilities of individual vesicles and quantal size, respectively (Fig. 5C-F). In contrast, expression of $G^{334}R$, $D^{335}A$, $Y^{471}A$, $Y^{471}F$, $I^{519}A$ and $Q^{559}A$ all significantly decreased the quantal size, the release probabilities of individual vesicles, the half width and the rise rate of each spike (Fig. 5C-F and Supplemental Fig. 5G-I). These results suggested that the interaction of PTP-MEG2 with NSF substrate is important for controlling vesicle size and the release probability of catecholamine secretion.

Unexpectedly, the PTP-MEG2 mutants showed different effects on the probability of the occurrence of the foot, which is an indicator of the initial opening of the fusion core (Fig. 5G). $G^{334}R$ mutation which disrupted the recognition of the N-terminal conformation of the peptide substrate of PTP-MEG2, and $D^{335}A$ and $Q^{559}A$, which are the determinants of pY+1 substrate specificity, significantly reduced the high potassium chloride-induced foot probability. The mutations of I^{519} and Y^{471}, which form specific interactions with the F^{85} of the NSF and are determinants of the C-terminal region of the central phospho-tyrosine involved in the substrate specificity of PTP-MEG2, showed no significant effect (Fig. 5B and Fig. 5G). These results indicated that PTP-MEG2 regulated the initial opening of the fusion core via a distinct structural basis from that of vesicle fusion, probably through dephosphorylating other unknown substrates. As $D^{335}A$ and $Q^{559}A$ of PTP-MEG2 maintained the occurrence of the foot probability, the unknown PTP-MEG2 substrate that regulates the fusion pore opening should have a small residue, such as G, A, S or T at the pY+1 position. Conversely, the unknown PTP-MEG2 substrate should have a less hydrophobic residue at the pY+2 position because $Y^{471}F$, $Y^{471}A$ and $I^{519}A$ of PTP-MEG2 had no significant effect on the foot probability.

Identification of new PTP-MEG2 substrates that contributed to the initial opening of the fusion core

The effects of PTP-MEG2 mutations along the PTP-MEG2/NSF-phospho-segment interface on catecholamine secretion indicated that not NSF but another PTP-MEG2 substrate with distinct sequence characteristics contributes to the regulation of “foot probability” (Fig. 5). We therefore utilize this key information to search for new potential PTP-MEG2 substrates

by bioinformatics methods (Fig. 6A). First, we searched for the keywords “fusion pore”, “secretory vesicle” and “tyrosine phosphorylation” using the functional protein association network STRING and the text mining tool PubTator, which resulted in a candidate list of 55 proteins. Second, we applied UniProt by selecting proteins located only in the membrane or vesicle, which limited the candidates to 28 members. Third, as our experiments were carried out in the adrenal gland, we used the Human Protein Atlas database for filtering, which narrowed the candidate list to 18 proteins. Finally, we exploited the post-translational-motif database PhosphoSitePlus to screen candidate proteins with potential phospho-sites that matched the sequence requirements at both the pY+1 position and the pY+2 position, which are “G, S, A, T, V, P” and “G, A, S, T, C, V, L, P, D, H”, respectively. These positions were further evaluated by surface exposure if a structure was available. The combination of these searches produced 11 candidate lists with predicted pY positions (Fig. 6B).

To biochemically characterize whether these proteins are substrates of PTP-MEG2, we transfected the plasmids encoding the cDNAs of these candidate proteins into PC12 cells, stimulated the cells with AngII, and performed a pull-down assay with the GST-MEG2-$D^{470}A$ trapping mutant or GST controls. The known PTP-MEG2 substrate NSF was used as a positive control. Notably, five candidates, including PACSIN1, MUNC18-1, VAMP7, DYNAMIN1 and SNAP25, showed specific interactions with PTP-MEG2 after AngII stimulation in PC12 cells (Fig. 6C and Supplemental Fig. 6A). Whereas the protein and mRNA of MUNC18-1, VAMP7, DYNAMIN1 and SNAP25 were readily detected in the adrenal medulla, PACSIN1 showed relatively lower expression than in the liver and brain (Supplemental Fig. 6B). Moreover, whereas MUNC18-1, VAMP7 and DYNAMIN1 strongly co-localized with PTP-MEG2 in the adrenal medulla (Fig. 6D-E and Supplemental Fig. 6C), the co-localization of SNAP25 and PACSIN1 with PTP-MEG2 was relatively weak (Supplemental Fig. 6D-E). MUNC18-1 and VAMP7 are candidate PTP-MEG2 substrates that were further strengthened by the fact that the high potassium chloride- or AngII-stimulated tyrosine phosphorylation of these proteins in the adrenal medulla was significantly dephosphorylated by PTP-MEG2 in vitro (Supplemental Fig. 7-1 A-I).

PTP-MEG2 regulated the initial opening of the fusion core through dephosphorylating MUNC18-1 at the pY^{145} site

The predicted PTP-MEG2 dephosphorylation site on MUNC18-1 (also called STXBP1) is Y^{145}, which is localized on the β sheet linker and forms extensive hydrophobic interactions with surrounding residues to tether the interface between domain 1 and domain 2 (Hu et al., 2011, Yang et al., 2015) (Fig. 7A and Supplemental Fig. 7-2A). Moreover, the phenolic-oxygen

of Y^{145} forms specific hydrogen bonds with the main chain amide of F^{540} and the main chain carbonyl oxygens of I^{539} and G^{568} (Fig. 7B). These key interactions might be involved in regulating the arrangement of the arc shape of the three domains of MUNC18-1. The phosphorylation of Y^{145} likely abolishes this H-bond network and changes its ability to associate with different snare complexes participating in vesicle fusion procedures (Fig. 7B). Interestingly, a missense mutation of MUNC18-1 $Y^{145}H$ was found to be associated with early infantile epileptic encephalopathy (Stamberger et al., 2017) (Fig. 7C).

Notably, the $Y^{145}H$ missense mutation may not be phosphorylated properly. We therefore overexpressed wild-type MUNC18-1, $Y^{145}A$, a non-phosphorylable mutant, and the disease-related $Y^{145}H$ mutant in PC12 cells stimulated with AngII and then examined their abilities to interact with PTP-MEG2. The GST pull-down results indicated that both MUNC18-1 $Y^{145}A$ and $Y^{145}H$, as well as another predicted substrate, VAMP7 $Y^{45}A/Y^{45}C$, had significantly decreased ability to associate with PTP-MEG2 (Fig. 7D). In contrast, mutations of the predicted phosphorylation sites of SNAP25 or DYNAMIN1, including SNAP25-$Y^{101}A$, DYNAMIN1-$Y^{354}A$ and DYNAMIN1- $Y^{597}A$, had no significant effect on their interactions with PTP-MEG2 (Supplemental Fig. 7-1 J). These results confirmed that pY^{145} is the major site of MUNC18-1 and VAMP7 pY^{45} for recognition by PTP-MEG2 (Fig. 7D).

We next infected primary chromaffin cells with a lentivirus encoding wild-type MUNC18-, the MUNC18-1 Y^{145}-tyrosine phosphorylation-deficient mutant $Y^{145}F$, the MUNC18-1 Y^{145}-tyrosine phosphorylation mimic mutant $Y^{145}E$ and the disease-related mutant $Y^{145}H$. Interestingly, either $Y^{145}E$ or $Y^{145}H$ significantly reduced the PSF and the SAF percentage of catecholamine secretion in response to AngII stimulation, whereas the phosphorylation-deficient mutant $Y^{145}F$ slightly increased the SAF percentage (Fig. 7E-F, and Supplemental Fig. 7-2 and 7-3). These results suggested that the tyrosine phosphorylation of Y^{145} impaired the initial opening of the fusion core in agonist-induced catecholamine secretion in primary chromaffin cells.

To further dissect the mechanism underlying the phosphorylation of MUNC18-1 Y^{145} as well as the disease-related mutant $Y^{145}H$ in the regulation of hormone secretion, we compared the interactions of wild-type and mutant MUNC18-1 with the binding partner SYNTAXIN1 (Lim et al., 2013). Importantly, both the phosphorylation mimic mutant MUNC18-1-$Y^{145}E$ and the disease-related mutant $Y^{145}H$ significantly impaired the interaction between MUNC18-1 and SYNTAXIN1 (Fig. 7G). These results suggested that the phosphorylation of Y^{145} of MUNC18-1 decreases the binding of MUNC18-1 to SYNTAXIN1, which plays an important role in the formation of the foot during catecholamine secretion. In contrast, the

dephosphorylation of pY^{145} of MUNC18-1 by PTP-MEG2 promoted initial pore opening and fusion.

Structural basis of the PTP-MEG2-MUNC18-1 interaction

The k_{cat}/K_m of PTP-MEG2 towards a phospho-segment derived from MUNC18-1-pY^{145} is very similar to that obtained with a phospho-segment derived from the known substrate pY^{83} site of NSF (Supplemental Fig. 3A-B and 8A). We therefore crystallized the PTP-MEG2 trapping mutant with the MUNC18-1-E^{141}-pY^{145}-S^{149} phospho-segment and determined the complex structure at 2.2 Å resolution (Table 1). The 2Fo-Fc electro-density map allowed the unambiguous assignment of seven residues of the phospho-MUNC18-1-E^{141}-pY^{145}-S^{149} segment in the crystal structure (Fig. 8A). Importantly, comparing with the phospho-NSF-E^{79}-pY^{83}-K^{87} segment, the phospho-MUNC18-1-E^{141}-pY^{145}-S^{149} displayed different interaction patterns with the residues in the PTP-MEG2 active site , forming new interactions with Q^{393} and R^{410} but looser interactions with Y^{471} and I^{519} (Fig. 8B). Whereas PTP-MEG2 Y^{471} formed extensive hydrophobic interactions with NSF-T^{84} and NSF-F^{85}, as well as a well-defined hydrogen bond (2.4 Å) with the carbonyl oxygen of NSF-pY^{83}, PTP-MEG2 Y^{471} formed only a weaker H-bond with the carbonyl oxygen of MUNC18-1-pY^{145} due to a 0.62 Å shift of Y^{471} away from the central pY substrate (Fig. 8C and Supplemental Fig. 8B). Similarly, PTP-MEG2 I^{519} did not form specific interactions with the MUNC18-1-E^{141}-pY^{145}-S^{149} segment except for the central pY. In contrast, PTP-MEG2 I^{519} formed specific hydrophobic interactions with NSF-T^{84} (Fig. 8D and Supplemental Fig. 8C). Consistently, mutations of PTP-MEG2 $Y^{471}A$, $Y^{471}F$ or $I^{519}A$ significantly decreased the phosphatase activity towards the phospho-NSF-E^{79}-pY^{83}-K^{87} segment (Fig. 3C) but had no significant effect on the phospho-MUNC18-1-E^{141}-pY^{145} -S^{149} segment (Fig. 8E). Combined with the results that PTP-MEG2 $Y^{471}A$, $Y^{471}F$ and $I^{519}A$ affect only the spike number and amount but show not the foot probability (Fig. 5B-G), these data suggested that PTP-MEG2 regulated intracellular vesicle fusion by modulating the NSF-pY^{83} phospho-state but regulated the process of vesicle fusion pore initiation by dephosphorylating MUNC18-1 at the pY^{145} site (Fig. 8F).

DISCUSSION

Posttranslational modifications of secretion machinery proteins are known as powerful ways to regulate exocytosis. In contrast to the well-characterized serine/threonine phosphorylation, the importance of tyrosine phosphorylation in exocytosis has only recently begun to be appreciated (Seino et al., 2009, Laidlaw et al., 2017, Jewell et al., 2011, Meijer et al., 2018, Gabel et al., 2019, Cijsouw et al., 2014). In addition to the phosphorylation of NSF

at its pY^{83} site, recent studies have shown that the tyrosine phosphorylation of MUNC18c at the pY^{219} and pY^{527} sites, Annexin-A2 at pY^{23}, and MUNC18-1 at pY^{473} actively participates in the vesicle release machinery to explicitly regulate exocytosis processes (Meijer et al., 2018, Jewell et al., 2011, Gabel et al., 2019). The tyrosine phosphorylation at specific sites of the signalling molecule is precisely regulated by tyrosine kinases and tyrosine phosphatases (Yu and Zhang, 2018, Tonks, 2006). Although tyrosine kinases such as the insulin receptor, Src and Fyn are acknowledged to play critical roles in hormone secretion (Soares et al., 2013, Jewell et al., 2011, Meijer et al., 2018, Oakie and Wang, 2018), only a very few tyrosine phosphatases that regulate the vesicle release machinery have been identified, and the structural basis of how these PTPs selectively dephosphorylate the key tyrosine phosphorylation sites governing exocytosis was unknown. In the current study, we demonstrated that PTP-MEG2 is an important regulator of hormone secretion from the medulla, using a selective PTP-MEG2 inhibitor in combination with cellular and electrochemical amperometric recording. The current study extended the regulatory role of PTP-MEG2 in various steps of exocytosis in hormone secretion beyond the previously known simple vesicle fusion step of the immune system (Huynh et al., 2004). We then determined the crystal structure of PTP-MEG2 in complex with the pY^{83} phospho-segment of the NSF, the key energy provider for disassembling fusion-incompetent cis SNARE complexes in the process of vesicle fusion in immunocytes (Huynh et al., 2004). The complex structure not only revealed the structural rearrangement after PTP-MEG2 in response to substrate binding, identifying Q^{559}:D^{335} as the key pair for substrate specificity of the pY+1 site, but also provided clues that PTP-MEG2 regulated the initial opening of the fusion pore through another unknown substrate. Fortunately, we were able to deduce the signature of the pY+1 and pY+2 positions of this unknown substrate by carefully inspecting the PTP-MEG2/phospho-NSF-E^{79}-pY^{83}-K^{87} complex structure and analysing the functional data of the PTP-MEG2 interface mutants. Further bioinformatics studies and cellular and physiological experiments enabled us to discover that PTP-MEG2 regulates the initial opening of the fusion pore by modulating the tyrosine phosphorylation states of MUNC18-1 at the pY^{145} site. Therefore, we have revealed that PTP-MEG2 regulates different steps of the exocytosis processes via distinct substrates. PTP-MEG2 regulates the vesicle size and vesicle-vesicle fusion step by dephosphorylating NSF at its NSF-pY^{83} site, whereas it regulates the process of large-dense-core vesicle fusion pore initiation and expansion by controlling MUNC18-1 at the pY^{145} site. Moreover, our studies highlight that the combination of structural determination and functional delineation of the interface mutants of the protein complex is a powerful approach to characterizing the signalling events and identifying unknown downstream signalling molecules.

Fusion pore opening and expansion is thought to be a complex process requiring the docking of apposed lipid bilayers and involvement of multiple proteins to form a hemi-fusion

diaphragm including SNAREs, MUNC18-1, and DYNAMIN (Hernandez et al., 2012, Sudhof and Rothman, 2009, Baker and Hughson, 2016, Zhao et al., 2016, Mattila et al., 2015, Jones et al., 2017). Dissection of the molecular mechanism underlying pore fusion dynamics in exocytosis is challenging because direct observation of this process is difficult to achieve due to the short expansion time and the tiny size of the pore (Baker and Hughson, 2016, Gaisano, 2017, Hong and Lev, 2014). MUNC18-1 and its closely related subfamily members have been demonstrated to participate in several processes during vesicle secretion by interacting with SNAREs, such as docking, priming and vesicle fusion (Korteweg et al., 2005, Fisher et al., 2001, Gulyas-Kovacs et al., 2007, Meijer et al., 2018, He et al., 2017, Chai et al., 2016, Sitarska et al., 2017, Cijsouw et al., 2014, Ma et al., 2015, Ma et al., 2013). Importantly, the tyrosine phosphorylation of MUNC18-1 at Y^{473} was recently reported as a key step in modulating vesicle priming by inhibiting synaptic transmission and preventing SNARE assembly (Meijer et al., 2018). In addition, the tyrosine phosphorylation of MUNC18c on Y^{521} was essential for the dissociation of MUNC18c and SYNTAXIN4 (Umahara et al., 2008). Moreover, the dephosphorylation of MUNC18-1-Y^{145} was suggested to be essential in maintaining the association between MUNC18-1 and SYNTAXIN1 (Lim et al., 2013), although its physiological relevance in exocytosis is not evaluated, and the endogenous modulator is not accurately defined. In the present study, we demonstrated that the MUNC18-1 $Y^{145}E$ phospho-mimic mutation, but not the non-phosphorylated mutation $Y^{145}F$, significantly decreased the PSF and the SAF probability. Consistently, only the specific PTP-MEG2 mutations that affect its activity towards MUNC18-1 reduced the PSF probability. The structural analysis of PTP-MEG2 in complex with MUNC18-1-pY^{145} and the enzymatic analysis further confirmed these observations. Collectively, these results indicate that the tyrosine phosphorylation of MUNC18-1 at its Y^{145} site and its dephosphorylation by PTP-MEG2 play essential roles in the regulation of the fusion pore opening process. Notably, the MUNC18-1 $Y^{145}H$ mutation is a known SNP that is associated with epileptic encephalopathy (Stamberger et al., 2017). $Y^{145}H$ behaves similarly to the MUNC18-1 phosphorylation mimic mutant $Y^{145}E$ by disrupting its interaction with SYNTAXIN1 and reducing the probability of PSF elicited by AngII in primary chromaffin cells. This observation provided a clue for the pathological effects of the MUNC18-1 $Y^{145}H$ mutation. In addition to MUNC18-1, we found that VAMP7 interacted with PTP-MEG2 via its Y^{45} tyrosine phosphorylation site. DYNAMIN-1, PASCIN1 and SNAP25 are also potential PTP-MEG2 substrates depending on specific cellular contexts. The functions of VAMP7 phosphorylation at the Y^{45} site and its dephosphorylation by PTP-MEG2, the interaction of PTP-MEG2 with DYNAMIN-1, etc. in the exocytosis process await further investigation.

Finally, by solving the two crystal structures of PTP-MEG2 in complex with two substrates, the phospho-NSF-E^{79}-pY^{83}-K^{87} segment and the phospho-MUNC18-1-E^{141}-pY^{145} -S^{149} segment, we revealed that PTP-MEG2 recognized these functionally different substrates through distinct

structural bases. Whereas K^{411}, Y^{471} and I^{519} contributed most to the selective interaction of PTP-MEG2 with NSF, another set of residues, including V^{393} and R^{410}, mediated the specific binding of PTP-MEG2 to MUNC18-1 (Fig. 8B). Most importantly, mutating Y^{471} and I^{519} to A significantly decreased the activity of PTP-MEG2 towards the phospho-NSF-E^{79}-pY^{83}-K^{87} segment but not the phospho-MUNC18-1-E^{141}-pY^{145}-S^{149} segment. The biochemical data agreed well with the functional data that PTP-MEG2 Y^{471}A and I^{519}A of PTP-MEG2 affected only the vesicle fusion procedure but not the fusion pore opening and expansion processes. These data not only indicate that PTP-MEG2 regulates different steps of exocytosis through different substrates in an explicit temporal and spatial context but also afforded important guidance for the design of selective PTP-MEG2 inhibitors according to the different interfaces between PTP-MEG2 and its substrates to explicitly regulate specific physiological processes, supporting the hypothesis of "substrate-specific PTP inhibitors" (Doody and Bottini, 2014). The design of such inhibitors will certainly help to delineate specific roles of PTP-MEG2 in different physiological and pathological processes.

In conclusion, we have found that PTP-MEG2 regulates two different processes of exocytosis during catecholamine secretion, namely, vesicle fusion and the opening and extension of the fusion pore, through two different substrates with distinct structural bases. We achieved this knowledge by determining the complex structure and performing functional delineation of the protein complex interface mutants. The present study supports the hypothesis that the tyrosine phosphorylation of secretion machinery proteins is an important category of regulatory events for hormone secretion and is explicitly regulated by protein tyrosine phosphatases, such as PTP-MEG2. Dissecting the molecular and structural mechanisms of such modulation processes will provide an in-depth understanding of the exocytosis process and guide further therapeutic development for exocytosis-related diseases, such as epileptic encephalopathy (Stamberger et al., 2017).

ACKNOWLEDGEMENTS

We thank Dr Michael Xi Zhu for stimulating discussions and critical reading of the manuscript. We thank Dr Zhongliang Zhu of University of Science and Technology of China, for his help in the crystal data collection, analysis and valuable discussion. We thank Yanmei Lu from Shandong jiaotong hospital, for her help with Transmission electron microscopy analysis. We thank Daolai Zhang and Mingliang Ma for their technical assistance in lentivirus packaging. We thank Yujing Sun and Zhixin Liu for their technical assistance in electrochemical recording. We acknowledge support from the National Key Basic Research Program of China Grant 2018YFC1003600 (to X.Y. and J.-P.S.), the National Natural Science Foundation of China

Grant 81773704 (to J.-P.S.), Grant 31701230 (to Z.Y.) and Grant 81601668 (to Y.-F.X.), the Shandong Provincial Natural Science Foundation, China (ZR2017BC045 to Z.Y.), the National Science Fund for Distinguished Young Scholars Grant 81825022 (to J.-P.S.), the National Science Fund for Excellent Young Scholars Grant 81822008 (to X. Y.) and the Rolling program of ChangJiang Scholars and Innovative Research Team in University Grant IRT_17R68 (to Y. S.).

AUTHOR CONTRIBUTIONS:

J.-P.S. and X.Y. conceived the whole research and initiated the project. J.-P.S., X.Y., Y.-F.X. and X.C. designed all of the experiments. J.-P.S. and X.Y. supervised the overall project design and execution. X.C., Y.-F.X., Z.Y., X.Y. and J.-P.S. participated in data analysis and interpretation. C.-H.L. and Y.-J.W. performed electrochemical experiments. M.C., Z.Y., P.X., K.-S.L. and Q.L. performed cell biology, molecular biology and biochemistry experiments. Z.-Y.Z. and S.Z. synthesized and purified the Compound 7 (PTP-MEG2 inhibitor) for us as a gift. X.-Z.Y. and Z.-L.J. performed substrate bioinformatics screening. Z.-Y.Z., W.-D.Z. and C.-H.W., C.W. and Y.-M.S. provided insightful idea and experimental designs. J.-P.S, Y.-F.X., X.C., and X.Y. wrote the manuscript. All of the authors have seen and commented on the manuscript.

DECLARATION OF INTERESTS

The authors declare no competing interests.

REFERENCE

ALONSO, A., SASIN, J., BOTTINI, N., FRIEDBERG, I., FRIEDBERG, I., OSTERMAN, A., GODZIK, A., HUNTER, T., DIXON, J. & MUSTELIN, T. 2004. Protein tyrosine phosphatases in the human genome. *Cell,* 117**,** 699-711.

ALVAREZ DE TOLEDO, G., FERNANDEZ-CHACON, R. & FERNANDEZ, J. M. 1993. Release of secretory products during transient vesicle fusion. *Nature,* 363**,** 554-8.

BAKER, R. W. & HUGHSON, F. M. 2016. Chaperoning SNARE assembly and disassembly. *Nat Rev Mol Cell Biol,* 17**,** 465-79.

BARR, A. J., UGOCHUKWU, E., LEE, W. H., KING, O. N., FILIPPAKOPOULOS, P., ALFANO, I., SAVITSKY, P., BURGESS-BROWN, N. A., MULLER, S. & KNAPP, S. 2009. Large-scale structural analysis of the classical human protein tyrosine phosphatome. *Cell,* 136**,** 352-63.

CHAI, Y. J., SIERECKI, E., TOMATIS, V. M., GORMAL, R. S., GILES, N., MORROW, I. C., XIA, D., GOTZ, J., PARTON, R. G., COLLINS, B. M., GAMBIN, Y. & MEUNIER, F. A. 2016. Munc18-1 is a molecular chaperone for alpha-synuclein, controlling its self-replicating aggregation. *J Cell Biol,* 214**,** 705-18.

CHEN, X. K., WANG, L. C., ZHOU, Y., CAI, Q., PRAKRIYA, M., DUAN, K. L., SHENG, Z. H., LINGLE, C. & ZHOU,

593 Z. 2005. Activation of GPCRs modulates quantal size in chromaffin cells through G(betagamma) and PKC.
594 *Nat Neurosci,* 8**,** 1160-8.
595 CHO, C. Y., KOO, S. H., WANG, Y., CALLAWAY, S., HEDRICK, S., MAK, P. A., ORTH, A. P., PETERS, E. C., SAEZ,
596 E., MONTMINY, M., SCHULTZ, P. G. & CHANDA, S. K. 2006. Identification of the tyrosine phosphatase
597 PTP-MEG2 as an antagonist of hepatic insulin signaling. *Cell Metab,* 3**,** 367-78.
598 CIJSOUW, T., WEBER, J. P., BROEKE, J. H., BROEK, J. A., SCHUT, D., KROON, T., SAARLOOS, I., VERHAGE,
599 M. & TOONEN, R. F. 2014. Munc18-1 redistributes in nerve terminals in an activity- and PKC-dependent
600 manner. *J Cell Biol,* 204**,** 759-75.
601 DITTMAN, J. S. & RYAN, T. A. 2019. The control of release probability at nerve terminals. *Nat Rev*
602 *Neurosci,* 20**,** 177-186.
603 DOODY, K. M. & BOTTINI, N. 2014. "PEST control": regulation of molecular barcodes by tyrosine
604 phosphatases. *Cell Res,* 24**,** 1027-8.
605 FISHER, R. J., PEVSNER, J. & BURGOYNE, R. D. 2001. Control of fusion pore dynamics during exocytosis
606 by Munc18. *Science,* 291**,** 875-8.
607 GABEL, M., DELAVOIE, F., ROYER, C., TAHOULY, T., GASMAN, S., BADER, M. F., VITALE, N. & CHASSEROT-
608 GOLAZ, S. 2019. Phosphorylation cycling of Annexin A2 Tyr23 is critical for calcium-regulated exocytosis
609 in neuroendocrine cells. *Biochim Biophys Acta Mol Cell Res,* 1866**,** 1207-1217.
610 GAISANO, H. Y. 2017. Recent new insights into the role of SNARE and associated proteins in insulin
611 granule exocytosis. *Diabetes Obes Metab,* 19 Suppl 1**,** 115-123.
612 GU, M., WARSHAWSKY, I. & MAJERUS, P. W. 1992. Cloning and expression of a cytosolic megakaryocyte
613 protein-tyrosine-phosphatase with sequence homology to retinaldehyde-binding protein and yeast
614 SEC14p. *Proc Natl Acad Sci U S A,* 89**,** 2980-4.
615 GULYAS-KOVACS, A., DE WIT, H., MILOSEVIC, I., KOCHUBEY, O., TOONEN, R., KLINGAUF, J., VERHAGE, M.
616 & SORENSEN, J. B. 2007. Munc18-1: sequential interactions with the fusion machinery stimulate vesicle
617 docking and priming. *J Neurosci,* 27**,** 8676-86.
618 HARADA, K., MATSUOKA, H., MIYATA, H., MATSUI, M. & INOUE, M. 2015. Identification of muscarinic
619 receptor subtypes involved in catecholamine secretion in adrenal medullary chromaffin cells by genetic
620 deletion. *Br J Pharmacol,* 172**,** 1348-59.
621 HE, E., WIERDA, K., VAN WESTEN, R., BROEKE, J. H., TOONEN, R. F., CORNELISSE, L. N. & VERHAGE, M.
622 2017. Munc13-1 and Munc18-1 together prevent NSF-dependent de-priming of synaptic vesicles. *Nat*
623 *Commun,* 8**,** 15915.
624 HERNANDEZ, J. M., STEIN, A., BEHRMANN, E., RIEDEL, D., CYPIONKA, A., FARSI, Z., WALLA, P. J., RAUNSER,
625 S. & JAHN, R. 2012. Membrane fusion intermediates via directional and full assembly of the SNARE
626 complex. *Science,* 336**,** 1581-4.
627 HONG, W. & LEV, S. 2014. Tethering the assembly of SNARE complexes. *Trends Cell Biol,* 24**,** 35-43.
628 HORNBECK, P. V., ZHANG, B., MURRAY, B., KORNHAUSER, J. M., LATHAM, V. & SKRZYPEK, E. 2015.
629 PhosphoSitePlus, 2014: mutations, PTMs and recalibrations. *Nucleic Acids Res,* 43**,** D512-20.
630 HU, S. H., CHRISTIE, M. P., SAEZ, N. J., LATHAM, C. F., JARROTT, R., LUA, L. H., COLLINS, B. M. & MARTIN,
631 J. L. 2011. Possible roles for Munc18-1 domain 3a and Syntaxin1 N-peptide and C-terminal anchor in
632 SNARE complex formation. *Proc Natl Acad Sci U S A,* 108**,** 1040-5.
633 HUYNH, H., BOTTINI, N., WILLIAMS, S., CHEREPANOV, V., MUSUMECI, L., SAITO, K., BRUCKNER, S.,
634 VACHON, E., WANG, X., KRUGER, J., CHOW, C. W., PELLECCHIA, M., MONOSOV, E., GREER, P. A., TRIMBLE,
635 W., DOWNEY, G. P. & MUSTELIN, T. 2004. Control of vesicle fusion by a tyrosine phosphatase. *Nat Cell*
636 *Biol,* 6**,** 831-9.

637 JEWELL, J. L., OH, E., RAMALINGAM, L., KALWAT, M. A., TAGLIABRACCI, V. S., TACKETT, L., ELMENDORF,
638 J. S. & THURMOND, D. C. 2011. Munc18c phosphorylation by the insulin receptor links cell signaling
639 directly to SNARE exocytosis. *J Cell Biol,* 193**,** 185-99.
640 JONES, D. M., ALVAREZ, L. A., NOLAN, R., FERRIZ, M., SAINZ URRUELA, R., MASSANA-MUNOZ, X., NOVAK-
641 KOTZER, H., DUSTIN, M. L. & PADILLA-PARRA, S. 2017. Dynamin-2 Stabilizes the HIV-1 Fusion Pore with
642 a Low Oligomeric State. *Cell Rep,* 18**,** 443-453.
643 KORTEWEG, N., MAIA, A. S., THOMPSON, B., ROUBOS, E. W., BURBACH, J. P. & VERHAGE, M. 2005. The
644 role of Munc18-1 in docking and exocytosis of peptide hormone vesicles in the anterior pituitary. *Biol*
645 *Cell,* 97**,** 445-55.
646 LAIDLAW, K. M. E., LIVINGSTONE, R., AL-TOBI, M., BRYANT, N. J. & GOULD, G. W. 2017. SNARE
647 phosphorylation: a control mechanism for insulin-stimulated glucose transport and other regulated
648 exocytic events. *Biochem Soc Trans,* 45**,** 1271-1277.
649 LI, H., YANG, F., LIU, C., XIAO, P., XU, Y., LIANG, Z., LIU, C., WANG, H., WANG, W., ZHENG, W., ZHANG, W.,
650 MA, X., HE, D., SONG, X., CUI, F., XU, Z., YI, F., SUN, J. P. & YU, X. 2016. Crystal Structure and Substrate
651 Specificity of PTPN12. *Cell Rep,* 15**,** 1345-58.
652 LIM, S. H., MOON, J., LEE, M. & LEE, J. R. 2013. PTPRT regulates the interaction of Syntaxin-binding
653 protein 1 with Syntaxin 1 through dephosphorylation of specific tyrosine residue. *Biochem Biophys Res*
654 *Commun,* 439**,** 40-6.
655 LIU, C. H., GONG, Z., LIANG, Z. L., LIU, Z. X., YANG, F., SUN, Y. J., MA, M. L., WANG, Y. J., JI, C. R., WANG,
656 Y. H., WANG, M. J., CUI, F. A., LIN, A., ZHENG, W. S., HE, D. F., QU, C. X., XIAO, P., LIU, C. Y., THOMSEN, A.
657 R., JOSEPH CAHILL, T., 3RD, KAHSAI, A. W., YI, F., XIAO, K. H., XUE, T., ZHOU, Z., YU, X. & SUN, J. P. 2017.
658 Arrestin-biased AT1R agonism induces acute catecholamine secretion through TRPC3 coupling. *Nat*
659 *Commun,* 8**,** 14335.
660 MA, C., SU, L., SEVEN, A. B., XU, Y. & RIZO, J. 2013. Reconstitution of the vital functions of Munc18 and
661 Munc13 in neurotransmitter release. *Science,* 339**,** 421-5.
662 MA, L., REBANE, A. A., YANG, G., XI, Z., KANG, Y., GAO, Y. & ZHANG, Y. 2015. Munc18-1-regulated stage-
663 wise SNARE assembly underlying synaptic exocytosis. *Elife,* 4.
664 MAGADMI, R., MESZAROS, J., DAMANHOURI, Z. A. & SEWARD, E. P. 2019. Secretion of Mast Cell
665 Inflammatory Mediators Is Enhanced by CADM1-Dependent Adhesion to Sensory Neurons. *Front Cell*
666 *Neurosci,* 13**,** 262.
667 MATTILA, J. P., SHNYROVA, A. V., SUNDBORGER, A. C., HORTELANO, E. R., FUHRMANS, M., NEUMANN,
668 S., MULLER, M., HINSHAW, J. E., SCHMID, S. L. & FROLOV, V. A. 2015. A hemi-fission intermediate links
669 two mechanistically distinct stages of membrane fission. *Nature,* 524**,** 109-113.
670 MEIJER, M., DORR, B., LAMMERTSE, H. C., BLITHIKIOTI, C., VAN WEERING, J. R., TOONEN, R. F., SOLLNER,
671 T. H. & VERHAGE, M. 2018. Tyrosine phosphorylation of Munc18-1 inhibits synaptic transmission by
672 preventing SNARE assembly. *EMBO J,* 37**,** 300-320.
673 NEHER, E. & BROSE, N. 2018. Dynamically Primed Synaptic Vesicle States: Key to Understand Synaptic
674 Short-Term Plasticity. *Neuron,* 100**,** 1283-1291.
675 OAKIE, A. & WANG, R. 2018. beta-Cell Receptor Tyrosine Kinases in Controlling Insulin Secretion and
676 Exocytotic Machinery: c-Kit and Insulin Receptor. *Endocrinology,* 159**,** 3813-3821.
677 ORTSATER, H., GRANKVIST, N., HONKANEN, R. E. & SJOHOLM, A. 2014. Protein phosphatases in
678 pancreatic islets. *J Endocrinol,* 221**,** R121-44.
679 PAN, C., LIU, H. D., GONG, Z., YU, X., HOU, X. B., XIE, D. D., ZHU, X. B., LI, H. W., TANG, J. Y., XU, Y. F., YU,
680 J. Q., ZHANG, L. Y., FANG, H., XIAO, K. H., CHEN, Y. G., WANG, J. Y., PANG, Q., CHEN, W. & SUN, J. P. 2013.

681 Cadmium is a potent inhibitor of PPM phosphatases and targets the M1 binding site. *Sci Rep,* 3**,** 2333.
682 SEINO, S., TAKAHASHI, H., FUJIMOTO, W. & SHIBASAKI, T. 2009. Roles of cAMP signalling in insulin
683 granule exocytosis. *Diabetes Obes Metab,* 11 Suppl 4**,** 180-8.
684 SITARSKA, E., XU, J., PARK, S., LIU, X., QUADE, B., STEPIEN, K., SUGITA, K., BRAUTIGAM, C. A., SUGITA, S.
685 & RIZO, J. 2017. Autoinhibition of Munc18-1 modulates synaptobrevin binding and helps to enable
686 Munc13-dependent regulation of membrane fusion. *Elife,* 6.
687 SOARES, H., HENRIQUES, R., SACHSE, M., VENTIMIGLIA, L., ALONSO, M. A., ZIMMER, C., THOULOUZE,
688 M. I. & ALCOVER, A. 2013. Regulated vesicle fusion generates signaling nanoterritories that control T
689 cell activation at the immunological synapse. *J Exp Med,* 210**,** 2415-33.
690 STAMBERGER, H., WECKHUYSEN, S. & DE JONGHE, P. 2017. STXBP1 as a therapeutic target for epileptic
691 encephalopathy. *Expert Opin Ther Targets,* 21**,** 1027-1036.
692 SUDHOF, T. C. 2004. The synaptic vesicle cycle. *Annu Rev Neurosci,* 27**,** 509-47.
693 SUDHOF, T. C. 2013. Neurotransmitter release: the last millisecond in the life of a synaptic vesicle.
694 *Neuron,* 80**,** 675-90.
695 SUDHOF, T. C. & ROTHMAN, J. E. 2009. Membrane fusion: grappling with SNARE and SM proteins.
696 *Science,* 323**,** 474-7.
697 SZKLARCZYK, D., FRANCESCHINI, A., WYDER, S., FORSLUND, K., HELLER, D., HUERTA-CEPAS, J.,
698 SIMONOVIC, M., ROTH, A., SANTOS, A., TSAFOU, K. P., KUHN, M., BORK, P., JENSEN, L. J. & VON MERING,
699 C. 2015. STRING v10: protein-protein interaction networks, integrated over the tree of life. *Nucleic Acids*
700 *Res,* 43**,** D447-52.
701 TESCHEMACHER, A. G. & SEWARD, E. P. 2000. Bidirectional modulation of exocytosis by angiotensin II
702 involves multiple G-protein-regulated transduction pathways in chromaffin cells. *J Neurosci,* 20**,** 4776-
703 85.
704 THUL, P. J., AKESSON, L., WIKING, M., MAHDESSIAN, D., GELADAKI, A., AIT BLAL, H., ALM, T., ASPLUND,
705 A., BJORK, L., BRECKELS, L. M., BACKSTROM, A., DANIELSSON, F., FAGERBERG, L., FALL, J., GATTO, L.,
706 GNANN, C., HOBER, S., HJELMARE, M., JOHANSSON, F., LEE, S., LINDSKOG, C., MULDER, J., MULVEY, C.
707 M., NILSSON, P., OKSVOLD, P., ROCKBERG, J., SCHUTTEN, R., SCHWENK, J. M., SIVERTSSON, A., SJOSTEDT,
708 E., SKOGS, M., STADLER, C., SULLIVAN, D. P., TEGEL, H., WINSNES, C., ZHANG, C., ZWAHLEN, M.,
709 MARDINOGLU, A., PONTEN, F., VON FEILITZEN, K., LILLEY, K. S., UHLEN, M. & LUNDBERG, E. 2017. A
710 subcellular map of the human proteome. *Science,* 356.
711 TONKS, N. K. 2006. Protein tyrosine phosphatases: from genes, to function, to disease. *Nat Rev Mol Cell*
712 *Biol,* 7**,** 833-46.
713 UMAHARA, M., OKADA, S., YAMADA, E., SAITO, T., OHSHIMA, K., HASHIMOTO, K., YAMADA, M., SHIMIZU,
714 H., PESSIN, J. E. & MORI, M. 2008. Tyrosine phosphorylation of Munc18c regulates platelet-derived
715 growth factor-stimulated glucose transporter 4 translocation in 3T3L1 adipocytes. *Endocrinology,* 149**,**
716 40-9.
717 VILAR, S., COZZA, G. & MORO, S. 2008. Medicinal chemistry and the molecular operating environment
718 (MOE): application of QSAR and molecular docking to drug discovery. *Curr Top Med Chem,* 8**,** 1555-72.
719 WANG, H. M., XU, Y. F., NING, S. L., YANG, D. X., LI, Y., DU, Y. J., YANG, F., ZHANG, Y., LIANG, N., YAO, W.,
720 ZHANG, L. L., GU, L. C., GAO, C. J., PANG, Q., CHEN, Y. X., XIAO, K. H., MA, R., YU, X. & SUN, J. P. 2014.
721 The catalytic region and PEST domain of PTPN18 distinctly regulate the HER2 phosphorylation and
722 ubiquitination barcodes. *Cell Res,* 24**,** 1067-90.
723 WANG, Y., VACHON, E., ZHANG, J., CHEREPANOV, V., KRUGER, J., LI, J., SAITO, K., SHANNON, P., BOTTINI,
724 N., HUYNH, H., NI, H., YANG, H., MCKERLIE, C., QUAGGIN, S., ZHAO, Z. J., MARSDEN, P. A., MUSTELIN, T.,

SIMINOVITCH, K. A. & DOWNEY, G. P. 2005. Tyrosine phosphatase MEG2 modulates murine development and platelet and lymphocyte activation through secretory vesicle function. *J Exp Med,* 202**,** 1587-97.

WEI, C. H., KAO, H. Y. & LU, Z. 2013. PubTator: a web-based text mining tool for assisting biocuration. *Nucleic Acids Res,* 41**,** W518-22.

WU, L. G., HAMID, E., SHIN, W. & CHIANG, H. C. 2014. Exocytosis and endocytosis: modes, functions, and coupling mechanisms. *Annu Rev Physiol,* 76**,** 301-31.

YANG, X., WANG, S., SHENG, Y., ZHANG, M., ZOU, W., WU, L., KANG, L., RIZO, J., ZHANG, R., XU, T. & MA, C. 2015. Syntaxin opening by the MUN domain underlies the function of Munc13 in synaptic-vesicle priming. *Nat Struct Mol Biol,* 22**,** 547-54.

YU, X., CHEN, M., ZHANG, S., YU, Z. H., SUN, J. P., WANG, L., LIU, S., IMASAKI, T., TAKAGI, Y. & ZHANG, Z. Y. 2011. Substrate specificity of lymphoid-specific tyrosine phosphatase (Lyp) and identification of Src kinase-associated protein of 55 kDa homolog (SKAP-HOM) as a Lyp substrate. *J Biol Chem,* 286**,** 30526-34.

YU, Z. H. & ZHANG, Z. Y. 2018. Regulatory Mechanisms and Novel Therapeutic Targeting Strategies for Protein Tyrosine Phosphatases. *Chem Rev,* 118**,** 1069-1091.

ZHANG, D., MARLIN, M. C., LIANG, Z., AHMAD, M., ASHPOLE, N. M., SONNTAG, W. E., ZHAO, Z. J. & LI, G. 2016. The Protein Tyrosine Phosphatase MEG2 Regulates the Transport and Signal Transduction of Tropomyosin Receptor Kinase A. *J Biol Chem,* 291**,** 23895-23905.

ZHANG, D. L., SUN, Y. J., MA, M. L., WANG, Y. J., LIN, H., LI, R. R., LIANG, Z. L., GAO, Y., YANG, Z., HE, D. F., LIN, A., MO, H., LU, Y. J., LI, M. J., KONG, W., CHUNG, K. Y., YI, F., LI, J. Y., QIN, Y. Y., LI, J., THOMSEN, A. R. B., KAHSAI, A. W., CHEN, Z. J., XU, Z. G., LIU, M., LI, D., YU, X. & SUN, J. P. 2018. Gq activity- and beta-arrestin-1 scaffolding-mediated ADGRG2/CFTR coupling are required for male fertility. *Elife,* 7.

ZHANG, S., LIU, S., TAO, R., WEI, D., CHEN, L., SHEN, W., YU, Z. H., WANG, L., JONES, D. R., DONG, X. C. & ZHANG, Z. Y. 2012. A highly selective and potent PTP-MEG2 inhibitor with therapeutic potential for type 2 diabetes. *J Am Chem Soc,* 134**,** 18116-24.

ZHAO, W. D., HAMID, E., SHIN, W., WEN, P. J., KRYSTOFIAK, E. S., VILLARREAL, S. A., CHIANG, H. C., KACHAR, B. & WU, L. G. 2016. Hemi-fused structure mediates and controls fusion and fission in live cells. *Nature,* 534**,** 548-52.

ZHOU, Z., MISLER, S. & CHOW, R. H. 1996. Rapid fluctuations in transmitter release from single vesicles in bovine adrenal chromaffin cells. *Biophys J,* 70**,** 1543-52.

FIGURE LEGENDS

Figure 1

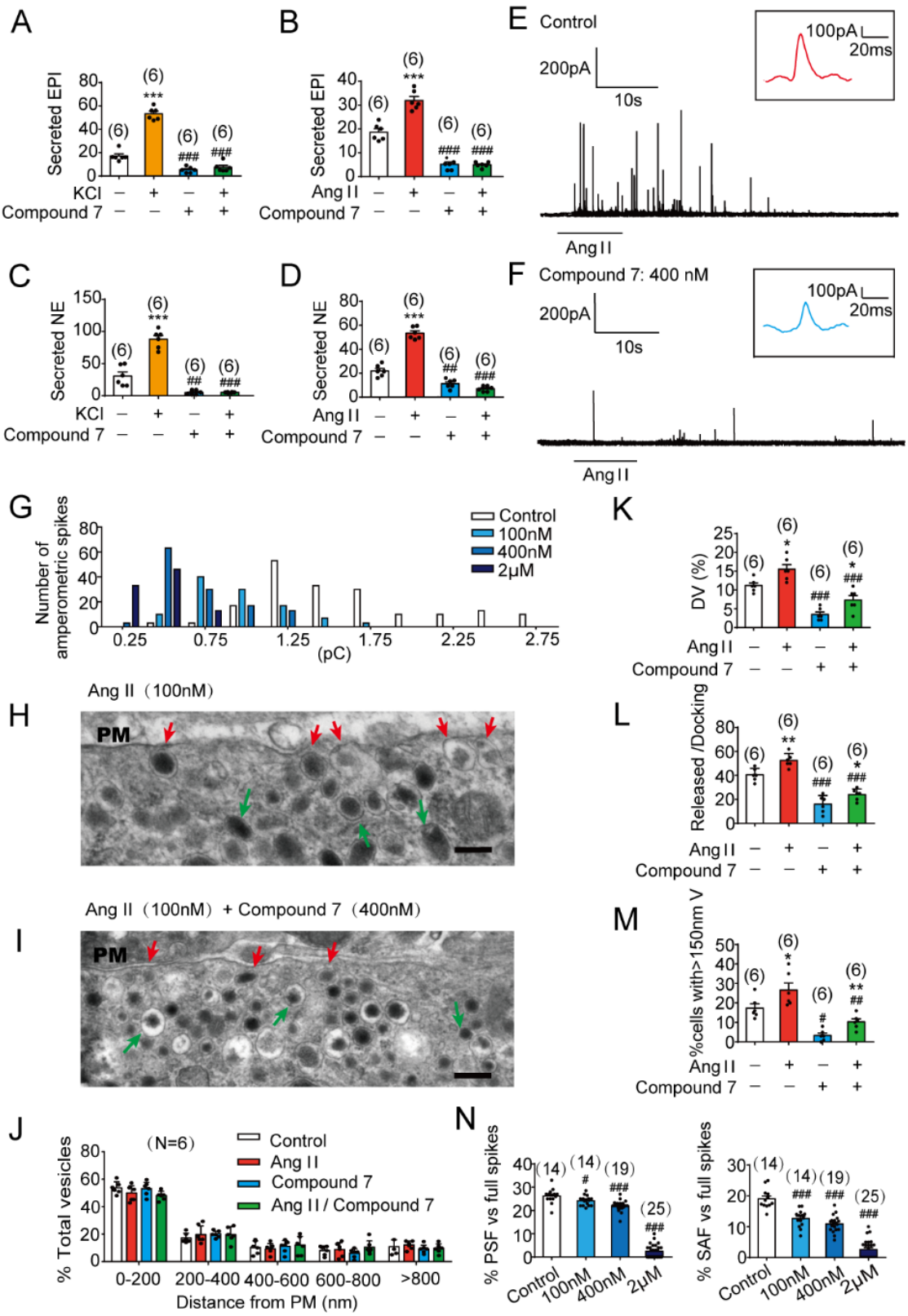

Figure 1. Inhibition of PTP-MEG2 reduced the spike amplitude and 'foot' probability of

catecholamine secretion.

(A-D). The epinephrine (A-B) or norepinephrine (C-D) secreted from the adrenal medulla was measured after stimulation with high KCl (70 mM) (A,C) or Angiotensin II (100 nM) (B,D) for 1 min, with or without pre-incubation with a specific PTP-MEG2 inhibitor (2 μM) for 2 hours. Data were obtained from 3 independent experiments and displayed as the mean ± SEM. **, P<0.01; ***, P<0.001: cells stimulated with KCl or AngII compared with un-stimulated cells. #, P<0.05; ##, P<0.01: cells pre-incubated with PTP-MEG2 inhibitors compared with control vehicles.

(E-F). Angiotensin II (AngII, 100 nM) induced amperometric spikes by primary mouse chromaffin cells after incubation with PTP-MEG2 inhibitor at different concentrations.

(G). The distribution of the quantal size of AngII (100 nM)-induced amperometric spikes by primary chromaffin cells after incubation with different concentrations of PTP-MEG2 inhibitor. Histograms show the number of amperometric spikes of different quantal sizes. Control: 182 spikes were calculated from 14 cells. 100 nM: 107 spikes were calculated from 14 cells. 400 nM: 126 spikes were calculated from 19 cells. 2 μM: 92 spikes were calculated from 25 cells.

(H and I). Secretory vesicles of primary chromaffin cells were examined by transmission electron microscopy before or after 100 nM AngII stimulation, with or without pre-incubation with 400 nM Compound 7. Scale bars: H, I, 150 nm.

(J). Vesicle numbers according to different distances from the plasma membrane were calculated in the presence or absence of 100 nM AngII or 400 nM Compound 7. PM stands for plasma membrane.

(K). The vesicles undergoing docking were counted and compared between subgroups after incubation with 100 nM AngII or 400 nM Compound 7. DV stands for docking vesicles.

(L). The ratio of released/docking vesicles was compared in the presence or absence of 100 nM AngII or 400 nM Compound 7.

(M). The percentage of vesicles with diameters greater than 150 nm was measured after 100 nM AngII stimulation or incubation with 400 nM Compound 7. Compound 7 significantly decreased vesicle size under AngII stimulation. In (K) (L) and (M), * and ** indicate P<0.05 and P<0.01, respectively, compared with the control group. #, ## and ### indicate P<0.05, <0.01 and <0.001 between incubated with the control vehicles and cells incubated with Compound 7. V stands for vesicles.

(N). The percentage of pre-spike foot (left panel) and stand-alone foot (right panel) were calculated after incubation with the indicated concentrations of Compound 7. * indicates P<0.05 compared with the control group. # indicates P<0.05 compared with the subgroup with AngII and without Compound 7. All statistical significance was calculated with one-way ANOVA. * indicates P<0.05 and *** indicates P<0.001.

Figure 2

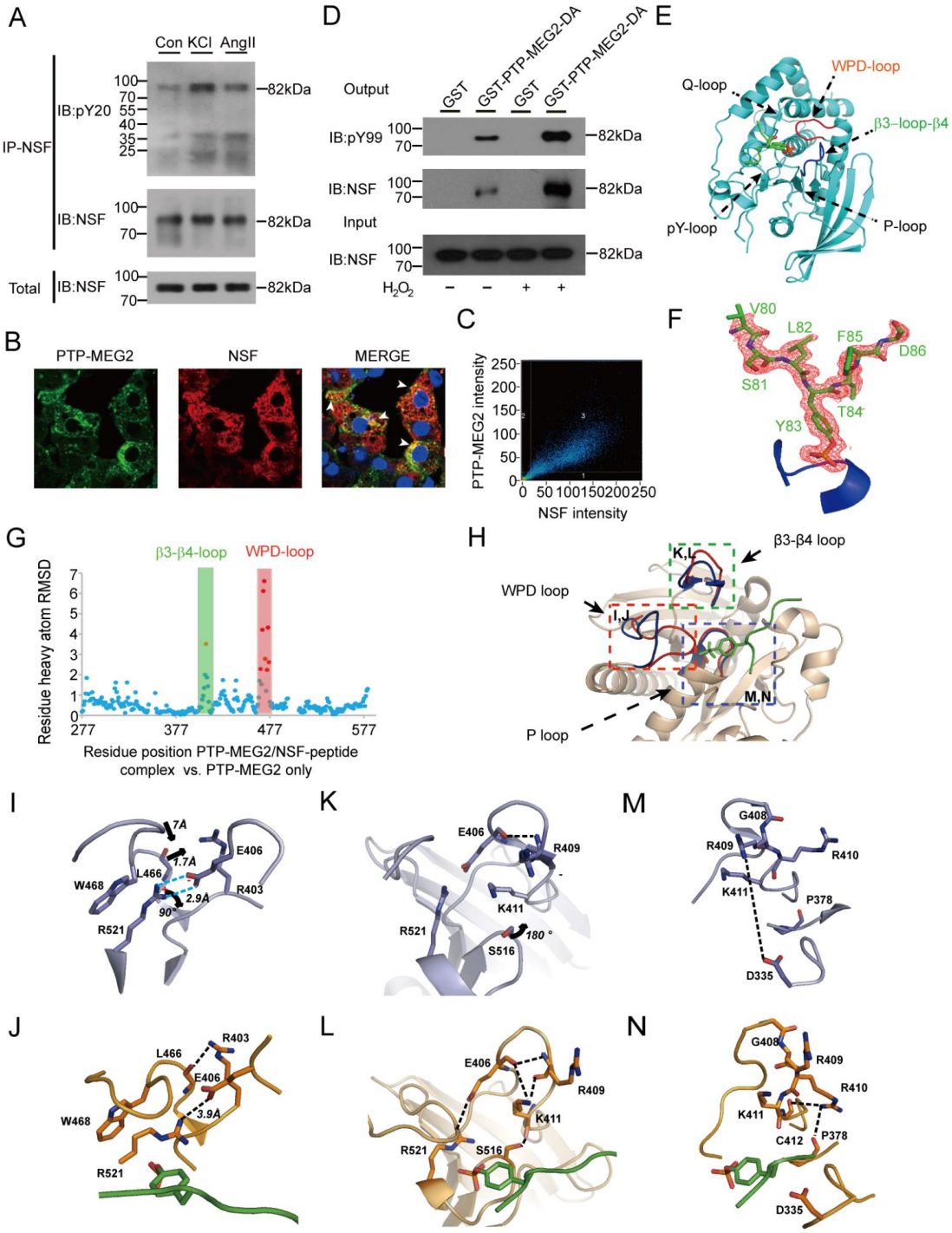

Figure 2 Interaction of PTP-MEG2 and tyrosine-phosphorylated NSF in the medulla and the crystal structure of the PTP-MEG2/phospho-NSF-segment complex.

(A). NSF was phosphorylated after stimulation with Ang II or KCl. Adrenal medulla cells were stimulated with 100 nM Ang II or 70 mM KCl for 1 min and lysed. NSF was immunoprecipitated with a specific NSF antibody coated with Protein A/G beads. A pan-

phospho-tyrosine antibody pY^{20} was used in Western blotting to detect the tyrosine-phosphorylated NSF in the adrenal medulla under different conditions.

(B). NSF was co-localized with PTP-MEG2 in the adrenal medulla. After stimulation with 100 nM Ang II, NSF and PTP-MEG2 in the adrenal medulla were visualized with immunofluorescence.

(C). Analysis of PTP-MEG2 and NSF fluorescence intensities by Pearson's correlation analysis. The Pearson's correlation coefficient was 0.7.

(D). Phosphorylated NSF interacted with PTP-MEG2. PC12 cells were transfected with FLAG-NSF. After stimulation of the cells with 100 μM H_2O_2, the potential PTP-MEG2 substrate in cell lysates was pulled down with GST-PTP-MEG2-D^{470}A or GST control.

(E). The overall structure of PTP-MEG2-C^{515}A/D^{470}A in complex with the NSF-pY^{83} phospho-segment.

(F). The 2Fo-Fc annealing omit map (contoured at 1.0σ) around the NSF-pY^{83} phospho-segment.

(G). Plot of distance RMSDs of individual residues between the crystal structures of the PTP-MEG2/NSF-pY^{83} phospho-peptide complex and the PTP-MEG2 native protein (PDB:2PA5).

(H). Superposition of the PTP-MEG2/NSF-pY^{83} phospho-peptide complex structure (red) on the PTP-MEG2 native protein structure (PDB:2PA5, blue). The structural rearrangement of the WPD loop and β3-loop-β4 is highlighted.

(I and J). The closure of the WPD loop and corresponding conformational changes in the inactive state (I) and the active state (J) of PTP-MEG2. The rotation of R^{521} leads to the movement of W^{468} and a corresponding 7 Å movement of the WPD loop.

(K and L). The structural rearrangement of β3-loop-β4 of PTP-MEG2 in the active state (L) compared with the inactive state (K). The disruption of the salt bridge between E^{406} and R^{521} contributed to the new conformational state of the N-terminal of β3-loop-β4.

(M and N). The conformational change of the P-loop of the inactive state (M) and the active state of PTP-MEG2 in response to NSF-pY^{83} segment binding (N). The disruption of the charge interaction between R^{409} and D^{335} resulted in the movement of the main chain from G^{408} to K^{411}.

Figure 3

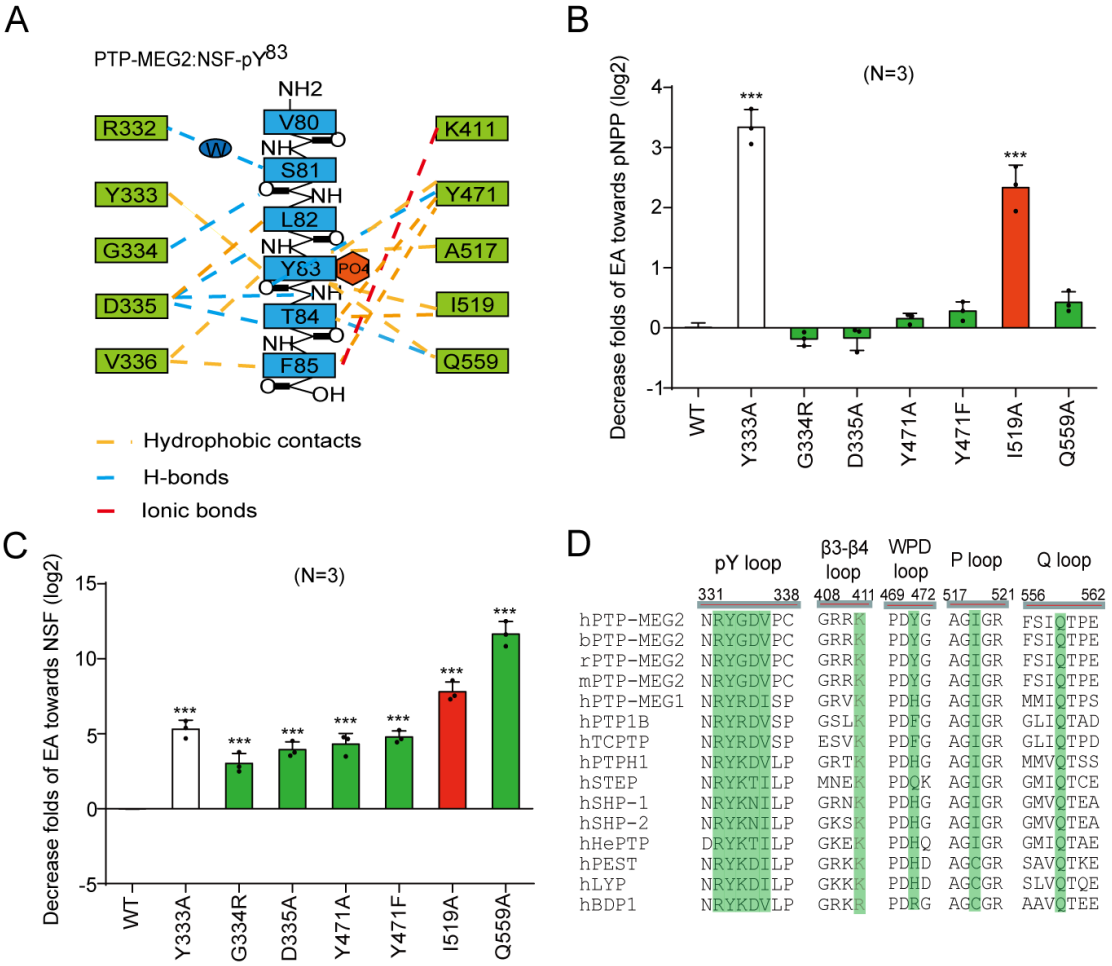

Figure 3. Molecular determinants of PTP-MEG2 interaction with the NSF-pY^{83} site.

(A). Schematic representation of interactions between PTP-MEG2 and the NSF-pY^{83} site.

(B). Relative values of the decreased phosphatase activities of different PTP-MEG2 mutants towards pNPP compared with wild-type PTP-MEG2.

(C). Fold-change decreases in the phosphatase activities of different PTP-MEG2 mutants towards the NSF-pY^{83} phospho-segment compared with wild-type PTP-MEG2.

(D). Sequence alignment of PTP-MEG2 from different species and with other PTP members. Important structural motifs participating in phosphatase catalysis or the recognition of the NSF-pY^{83} site are shown, and key residues contributing to the substrate specificity are highlighted. B-C, the statistical significance was calculated with Student's t test. *** P<0.001; PTP-MEG2 mutants compared with the control.

Figure 4

A

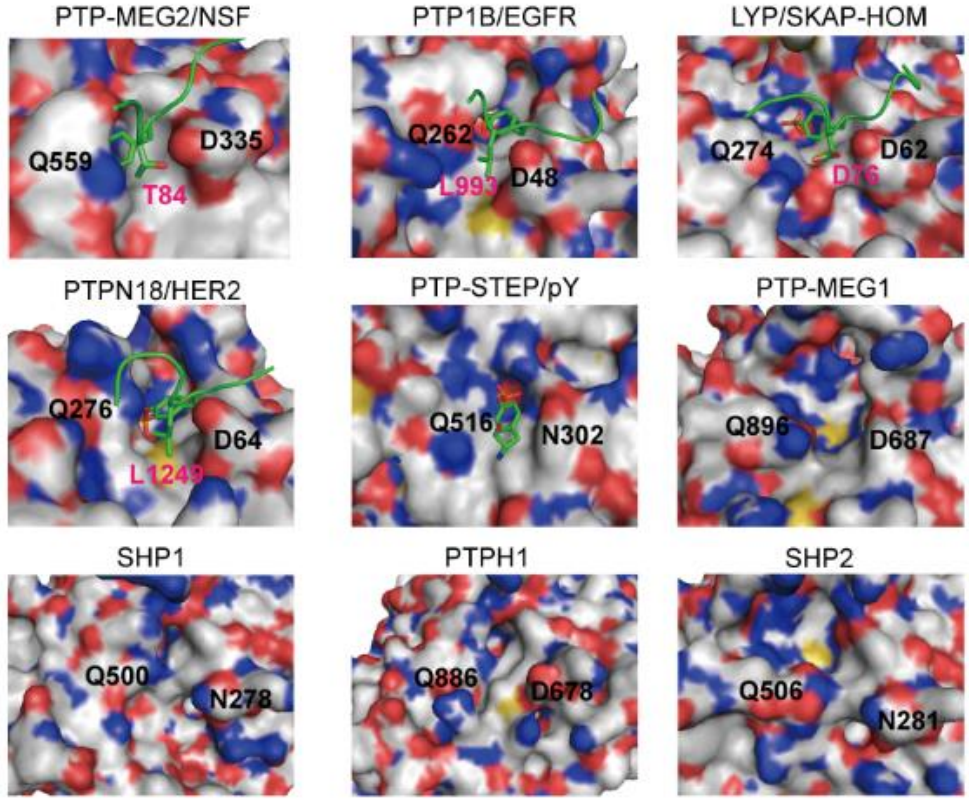

B

Complex	PDB code	pY+1	Distance(Cβ)	
PTP-MEG2/NSF(pY83)		T	10.42	D335:Q559
PTP1B/EGFR(pY992)	1EEN	L	11.46	D48:Q262
LYP/SKAP-HOM(pY75)	3OMH	D	11.32	D63:Q274
PTPN18/HER2(pY1248)	4GFU	L	11.89	D64:Q276
PTP-STEP/pY	2CJZ		12.43	N312:Q516
PTP-MEG1	2I75		11.16	D687:Q896
SHP1	4HJQ		12.27	N278:Q500
PTPH1	4QUN		12.35	D678:Q886
SHP2	3B7O		12.44	N281:Q506

Figure 4. The tip opening of the pY+1 pocket is critical for PTP-MEG2 substrate specificity.

(A). Surface representations of the complex structures of PTP-MEG2-C^{515}A/D^{470}A/NSF-pY^{83}, PTP1B-C^{215}A/IRK-$pY^{1162/1163}$ (PDB:1EEN), LYP-C^{227}S/SKAP-HOM-pY^{75} (PDB:3OMH), PTPN18-C^{229}S/HER2-pY^{1248} (PDB:4GFU), and PTP-STEP/pY (PDB:2CJZ). Crystal structures of PTP-MEG1 (PDB:2I75), SHP1 (PDB:4HJQ), PTPH1 (PDB:4QUN) and SHP2

(PDB: 3B7O). The pY+1 sites are highlighted.

(B). Summary of the distance between the Cβ atoms of D^{335} and Q^{559} (corresponding to PTP-MEG2 number) of the pY+1 pocket in PTP-MEG2 and other classical non-receptor PTPs bearing the same residues at similar positions.

Figure 5

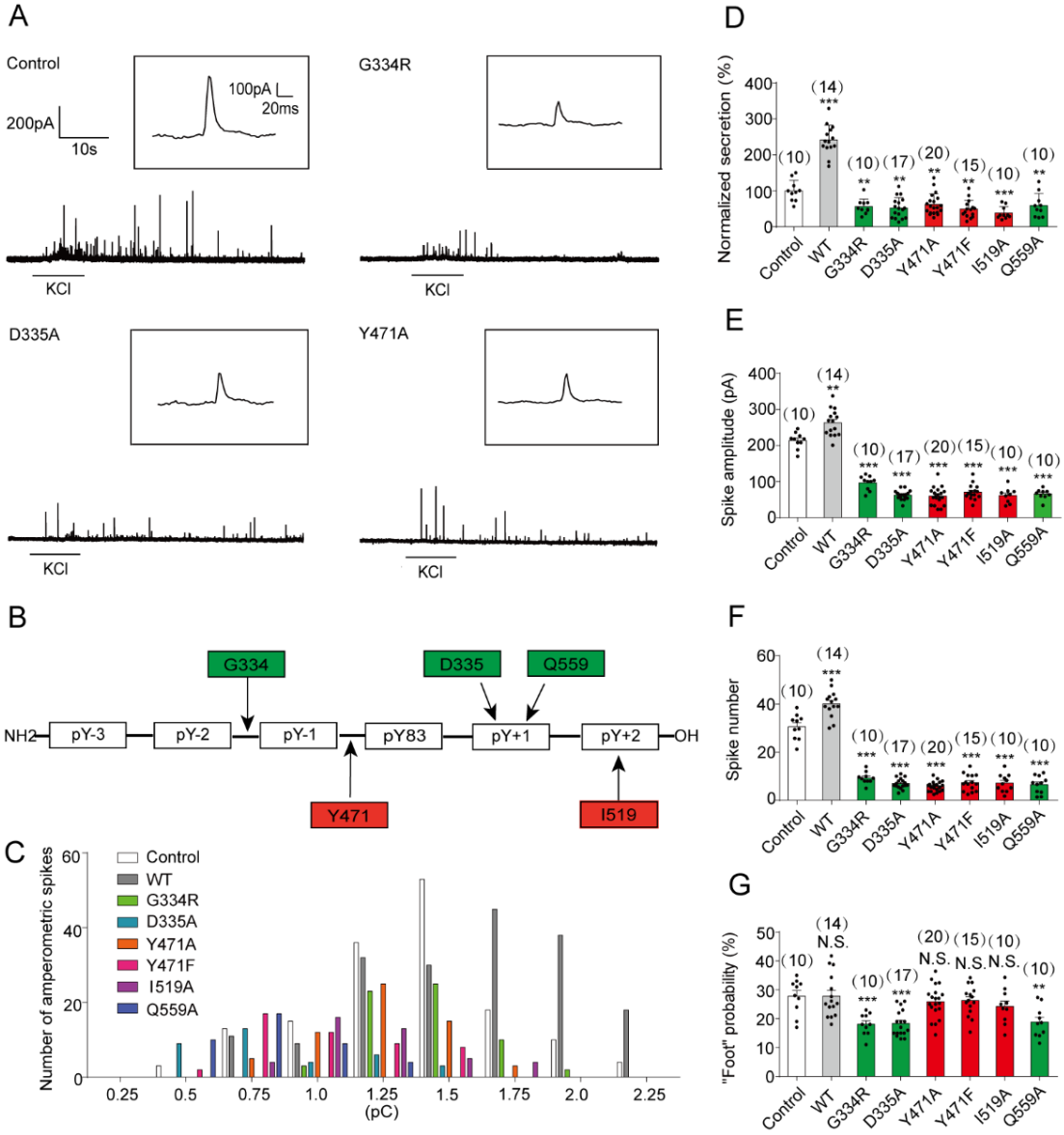

Figure 5. Effects of different PTP-MEG2 mutants on properties of catecholamine secretion from primary chromaffin cells.

(A). Primary mouse chromaffin cells were transduced with a lentivirus containing the gene for wild-type PTP-MEG2 or different mutants with a GFP tag at the C-terminus. Positive transfected cells were confirmed with green fluorescence and selected for electrochemical analysis. Typical amperometric current traces evoked by KCl (70 mM for 5 seconds) in the

control (transduced with control vector) (top left panel), $G^{334}R$ (top right panel), $D^{335}A$ (bottom left panel), and $Y^{471}A$ (bottom right panel) are shown.

(B). The schematic diagram shows key residues of PTP-MEG2 defining the substrate specificity adjacent to the pY^{83} site of NSF.

(C). The distribution of the quantal size of chromaffin cells transduced with lentivirus containing the genes encoding different PTP-MEG2 mutants. Data are from 625 amperometric spikes of 105 chromaffin cells.

(D). Statistical diagram of the quantal size in Fig. 5A. The secretion amount of each group was standardized with respect to the control group.

(E-G). Calculated parameters of secretory dynamics, including the spike amplitude (E), spike number (F), and foot frequency (G).

D-G, the statistical significance was calculated with Student's t test. *, $P<0.05$; **, $P<0.01$; *** $P<0.001$: PTP-MEG2 mutants compared with the control.

Figure 6

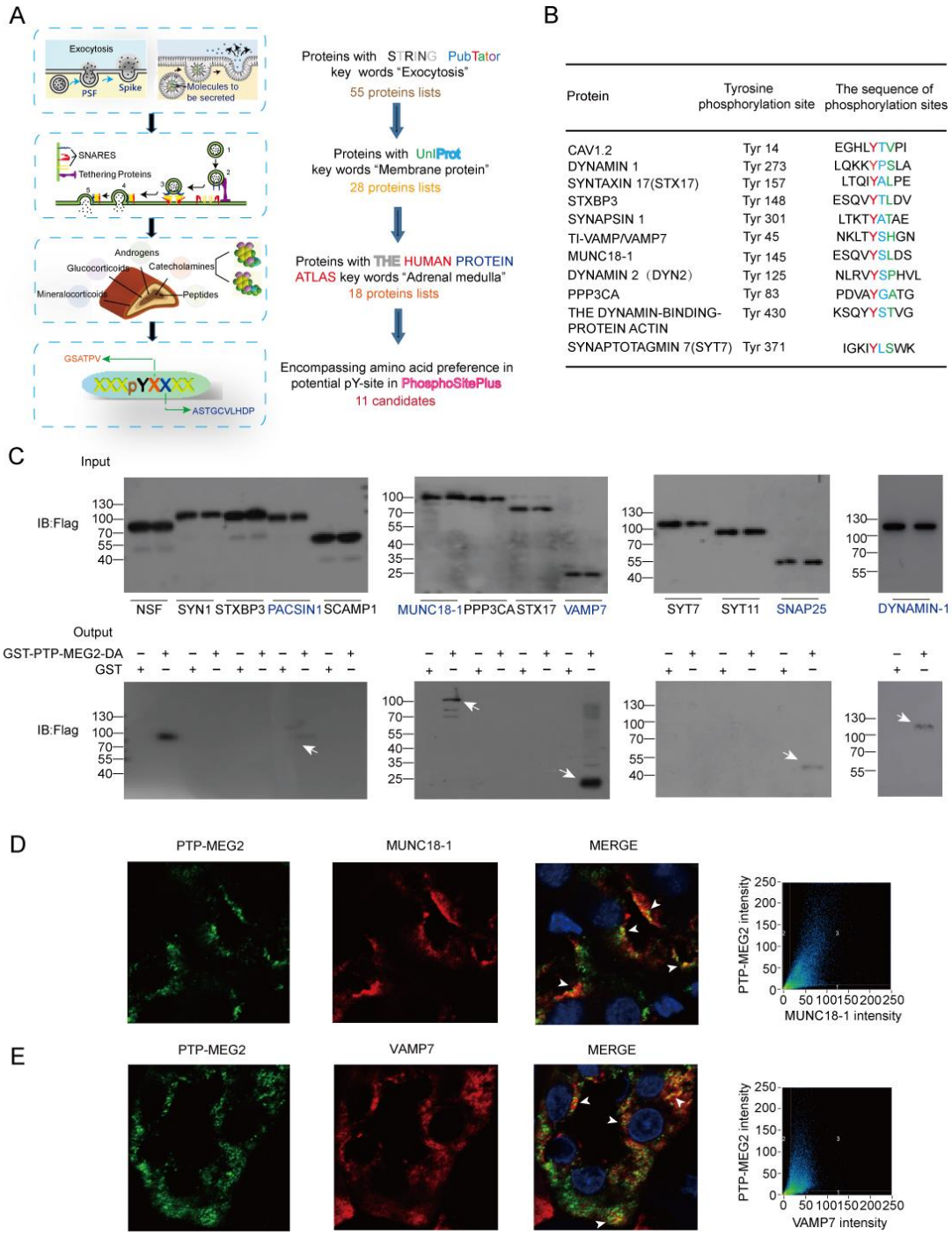

Protein	Tyrosine phosphorylation site	The sequence of phosphorylation sites
CAV1.2	Tyr 14	EGHLYTVPI
DYNAMIN 1	Tyr 273	LQKKYPSLA
SYNTAXIN 17(STX17)	Tyr 157	LTQIYALPE
STXBP3	Tyr 148	ESQVYTLDV
SYNAPSIN 1	Tyr 301	LTKTYATAE
TI-VAMP/VAMP7	Tyr 45	NKLTYSHGN
MUNC18-1	Tyr 145	ESQVYSLDS
DYNAMIN 2（DYN2）	Tyr 125	NLRVYSPHVL
PPP3CA	Tyr 83	PDVAYGATG
THE DYNAMIN-BINDING-PROTEIN ACTIN	Tyr 430	KSQYYSTVG
SYNAPTOTAGMIN 7(SYT7)	Tyr 371	IGKIYLSWK

Figure 6. Identification of potential candidate substrates of PTP-MEG2 that participate in fusion pore initiation and expansion.

(A). Flowchart for the workflow to predict the candidate substrates of PTP-MEG2 during fusion pore initiation and expansion. A total of 55 proteins were enriched with the functional protein association network STRING and the text mining tool PubTator by searching the keywords

“fusion pore”, “secretory vesicle” and “tyrosine phosphorylation”. These proteins were filtered with UniProt by selecting proteins located only in the membrane or vesicle, which resulted in 28 candidates. The Human Protein Atlas database was then applied to exclude proteins with no expression in the adrenal gland. Finally, we used the post-translational-motif database PhosphoSitePlus to screen candidate proteins with potential phospho-sites that matched our sequence motif prediction at the pY+1 or pY+2 positions.

(B). After the bioinformatics analysis, a total of 11 candidate PTP-MEG2 substrates that may participate in fusion pore initiation and expansion and their potential phospho-sites were displayed.

(C). The GST pull-down assay suggested that PACSIN1, MUNC18-1, VAMP7, SNAP25 and DYNAMIN-1 directly interact with PTP-MEG2. PC12 cells were transfected with plasmids of candidate substrates, including SYN1, STXBP 3, PACSIN 1, SCAMP 1, MUNC18-1, PPP3CA, STX17, VAMP7, SYT7, SYT11, SNAP 25 and DYNAMIN-1, and stimulated with 100 nM AngII. The tyrosine phosphorylation of these proteins was verified by specific anti-pY antibodies (Supplemental Fig. 7-1 A-I). The potential substrates of PTP-MEG2 in cell lysates were pulled down with a GST-PTP-MEG2-D^{470}A trapping mutant and then detected by Western blotting.

(D-E). Co-immunostaining assays of PTP-MEG2 with potential substrates in the adrenal medulla. MUNC18-1 and VAMP7 all showed strong co-localization with PTP-MEG2 after 100 nM AngII stimulation in the adrenal medulla. The Pearson’s correlation coefficients for D and E were 0.61 and 0.65, respectively. The co-immunostaining results of PTP-MEG2 with other potential substrates are shown in Supplemental Fig. 6.

Figure 7

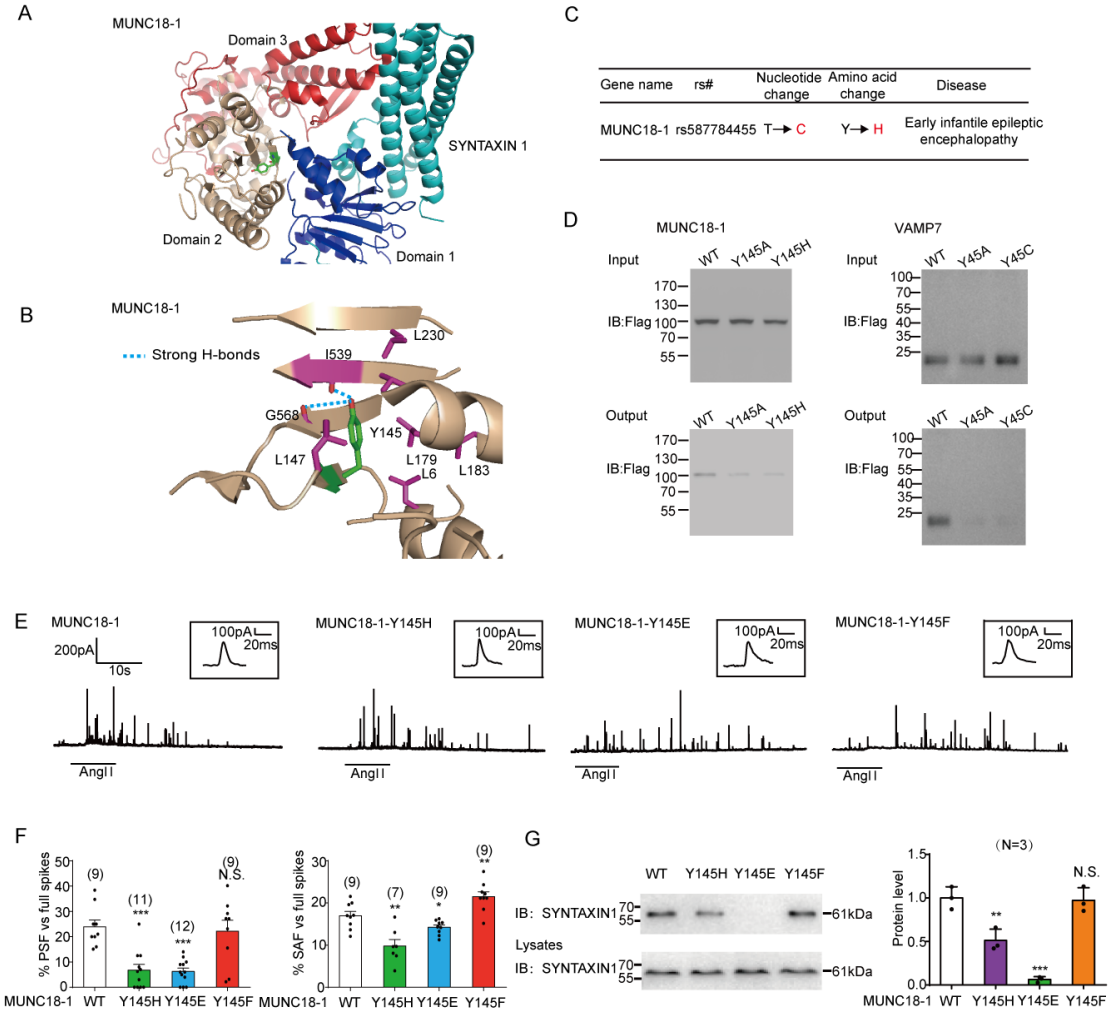

Figure 7. Dephosphorylation of MUNC18-1 at the pY^{145} site by PTP-MEG2 determines the "foot" probability of catecholamine secretion from chromaffin cells.

(A). Structural representation and location of MUNC18-1-Y^{145} in the complex structure of MUNC18-1-SYNTAXIN1 (PDB: 3PUJ).

(B). Detailed structural representation of Y^{145} and its interacting residues. Y^{145} of MUNC18-1 interacts with the main chain carboxylic oxygen of residues I^{539} and G^{568} and forms hydrophobic interactions with L^{6}, I^{539}, L^{147}, L^{179}, L^{183}, and L^{230} to tether the arc shape of the three domains of MUNC18-1 (PDB: 3PUJ).

(C). Association analysis of SNPs of MUNC18-1 with human disease.

(D). Interactions of the PTP-MEG2-trapping mutants with the MUNC18-1-Y^{145} mutants (left) and VAMP7-Y^{45} mutants (right). PC12 cells were transfected with FLAG-MUNC18-1-Y^{145} and different mutations of the FLAG-MUNC18-1-Y^{145}A or Y^{145}H mutants, the FLAG-VAMP7-Y^{45} and different mutations of the FLAG-VAMP7-Y^{45}A or Y^{45}C mutants 24 hours before

stimulation with 100 nM AngII, respectively. The cell lysates were then incubated with GST-PTP-MEG2-D^{470}A for 4 hours with constant rotation. The potential PTP-MEG2 substrates were pulled down by GST-beads, and their levels were examined by the FLAG antibody with Western blotting.

(E). Primary chromaffin cells were transduced with lentivirus containing the gene encoding wild-type MUNC18-1 or different mutants. These cells were stimulated with 100 nM AngII. The amperometric spikes were detected with CFE. Typical amperometric traces are shown.

(F). The percentages of pre-spike foot (left) and stand-alone foot (right) for wild-type MUNC18-1 or different mutants were calculated.

(G). The MUNC18-1-Y^{145} mutation decreased the interaction between MUNC18-1 and SYNTAXIN1. PC12 cells were transfected with plasmid carrying SYNTAXIN-1. The proteins in cell lysates were pulled down with purified GST-MUNC18-1-Y^{145} and the GST-MUNC18-1-Y^{145}H/E/F, and detected with SYNTAXIN1 antibody. The right histogram shows the quantified protein levels. ** and *** represent $P<0.01$ and $P<0.001$ compared with the control groups.

Figure 8

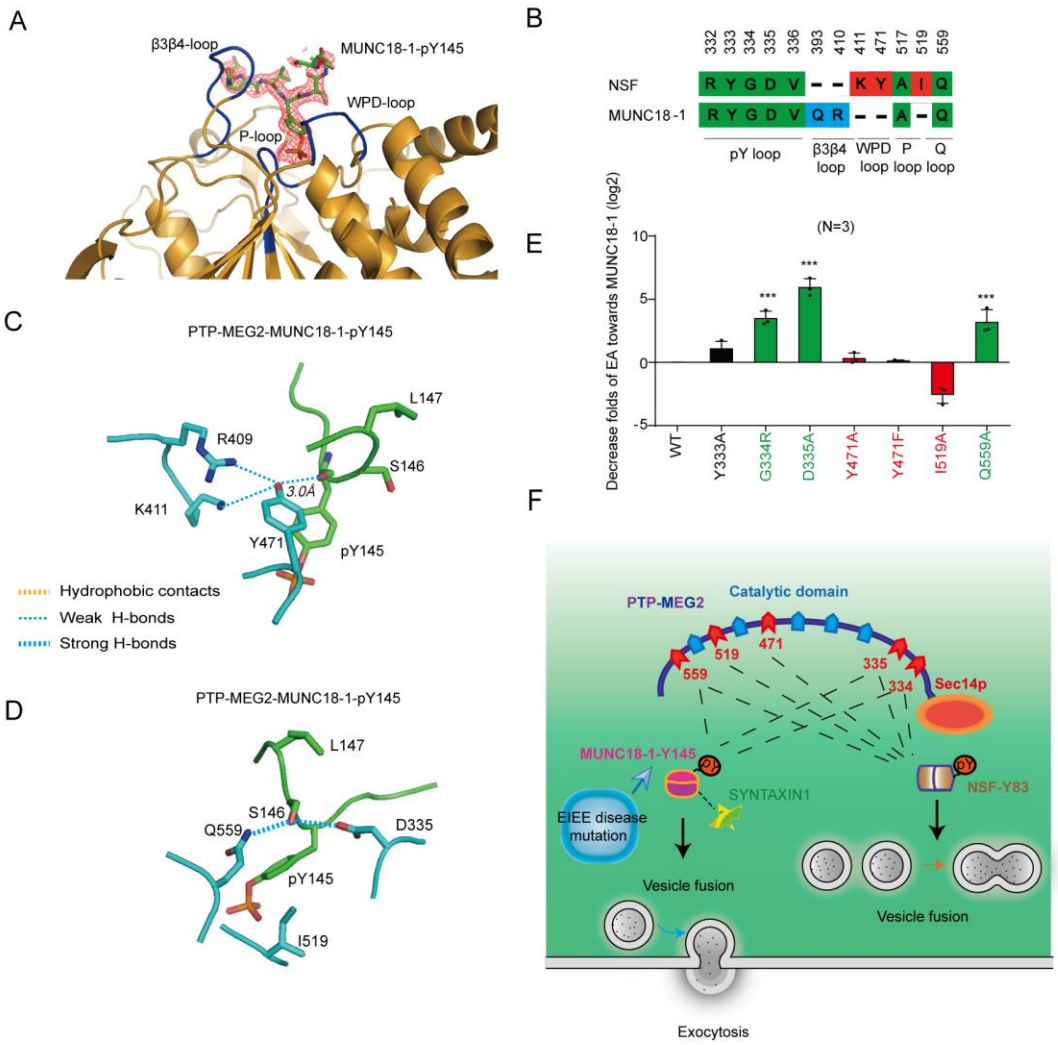

Figure 8. The structural details of the PTP-MEG2-MUNC18-1-Y^{145} interaction and catalytic bias of PTP-MEG2 towards NSF-pY^{83} and MUNC18-1-pY^{145}

(A). The 2Fo-Fc annealing omit map (contoured at 1.0σ) around MUNC18-1-pY^{145} phospho-segment.

(B). Comparison of residues of PTP-MEG2 interacting with NSF and MUNC18-1. Amino acid residues of NSF and MUNC18-1 are coloured as follows: green, residues interacting with both NSF and MUNC18-1; red, residues strongly contributing to NSF recognition; blue, residues strongly contributing to MUNC18-1 interaction.

(C). The structural alteration of the interactions surrounding Y^{471} of PTP-MEG2 with the MUNC18-1-pY^{145} site.

(D). The structural alteration of the interactions surrounding I^{519} of PTP-MEG2 with the MUNC18-1-pY^{145} site.

(E). Relative phosphatase activities of different PTP-MEG2 mutants towards the MUNC18-1-

pY^{145} phospho-segment compared with wild-type PTP-MEG2.

(F). Schematic illustration of the PTP-MEG2-regulated processes of vesicle fusion and secretion in chromaffin cells via the dephosphorylation of different substrates with distinct structural basis. PTP-MEG2 regulates vesicle fusion and vesicle size during the catecholamine secretion of adrenal gland by modulating the phosphorylation state of the pY^{83} site of NSF, which relies on the key residues G^{334}, D^{335} (pY loop), Y^{471} (WPD loop), I^{519} (P-loop) and Q^{559} (Q loop). PTP-MEG2 regulates the fusion pore initiation and expansion procedures of catecholamine secretion by the adrenal gland (also designated as foot probability) by modulating the newly identified substrate MUNC18-1 at its pY^{145} site, a distinct structural basis from that of its regulation of NSF phosphorylation. Defects in the dynamic tyrosine phosphorylation of the MUNC18-1 pY^{145} site and its interaction with PTP-MEG2 may contribute to early infantile epilepsy encephalopathy (EIEE).

STAR★METHODS

KEY RESOURCES TABLE

REAGENT or RESOURCE	SOURCE	IDENTIFIER
Antibodies		
NSF Antibody	Proteintech	Cat # 21171-1-AP
MUNC18-1 Antibody	Proteintech	Cat # 11459-1-AP
VAMP7 Antibody	Proteintech	Cat # 22268-1-AP
SNAP25 Antibody	Proteintech	Cat # 14903-1-AP
PACSIN1 Antibody	Proteintech	Cat # 13219-1-AP
SYNTAXIN1a Antibody	Proteintech	Cat # 66437-1-lg
pTyr(PY20) Antibody	Santa Cruz	Cat # sc-508
pTyr(PY99) Antibody	Santa Cruz	Cat # sc-7020
FLAG Antibody	Cell Signaling Technology	Cat # 2368
GAPDH Antibody	Cell Signaling Technology	Cat # 5174
PTP-MEG2 Antibody	R&D Systems	Cat # MAB2668
DYNAMIN1 Antibody	Abcam	Cat # MAB52611
Chemicals, Peptides, and Recombinant Proteins		

Anti-GST-tag beads	TransGen Biotech Co., Ltd	Cat # DP201
Protein A/G-PLUS-Agarose	Santa Cruz	Cat # sc-2003
Ni-NTA Agarose	Thermo Fisher scientific	Cat # R90101
The phospho-peptide of NSF "EVSLpYTFDK"	China Peptides Co., Ltd	N/A
The phospho-peptide of MUNC18-1 "ESQVpYSLDS"	China Peptides Co., Ltd	N/A
Mouse EPI ELISA Kit	Shanghai Jianglai Co.,Ltd	JL11194-48T
Mouse NE ELISA Kit	Shanghai Jianglai Co.,Ltd	JL13969-96T
Angiotensin II (HDRVYIHPF-OH)	China Peptides Co., Ltd	N/A
Compound 7(PTP-MEG2 inhibitor)	Synthesized as previously described(Zhang et al., 2012)	
Experimental Models: Cell Lines		
293	ATCC	CRL-1573
293T	ATCC	CRL-3216
PC12	ATCC	CRL-1721
Software and Algorithms		
PyMol	Schrödinger	https://www.pymol.org/
CCP4i	Instruct Associate Centre for Integrated Structural Biology	http://www.ccp4.ac.uk/
Phenix	The PHENIX Industrial Consortium	https://www.phenix-online.org
Igor	Fourier Transform	https://www.wavemetrics.com/
Prism	GraphPad	http://www.graphpad.com

CONTACT FOR REAGENT AND RESOURCE SHARING

Further information and requests for resources and reagents should be directed to and will be fulfilled by the Lead Contact, Professor Xiao Yu. (yuxiao@sdu.edu.cn) or Jinpeng Sun (sunjinpeng@bjmu.edu.cn)

EXPERIMENTAL MODEL AND SUBJECT DETAILS

Cell Culture

The HEK293 cell lines, the 293T cell lines and PC12 cell lines were originally obtained from the American Type Culture Collection (ATCC). The HEK293 cell lines and 293T cell lines were grown in DMEM with 10% FBS (Gibco, Grand Island, NY, US) and 1% penicillin/streptomycin at 37 °C. PC12 cells were maintained at 37 °C in DMEM medium containing 10% FBS (Gibco, US), 5% donor equine serum (Gibco, US) and 1% penicillin/streptomycin.

METHOD DETAILS

Constructs

Sequences of PTP-MEG2 catalytic domain were subcloned into PET-15b expression vector with an N-terminal His tag or PGEX-6P-2 expression vector containing an N-terminal GST tag. The mutations of PTP-MEG2 were constructed by the Quikchange kit from Stratagene .

Plasmid	Primer sequence
His-PTPMEG2-333Y-A	F:5'GAAACCTAGAGAAAAACCGTGCGGGGGATGTACCCTGCCTGGAC 3' R:5'GTCCAGGCAGGGTACATCCCCCGCACGGTTTTTCTCTAGGTTTC 3'
His-PTPMEG2-334G-R	F: 5' CTAGAGAAAAACCGTTATCGTGATGTACCCTGCCTGGAC 3' R: 5' GTCCAGGCAGGGTACATCACGATAACGGTTTTTCTCTAG 3'
His-PTPMEG2-	F: 5' GAAAAACCGTTATGGGGCGGTACCCTGCCTGGACC 3' R: 5' GGTCCAGGCAGGGTACCGCCCCATAACGGTTTTTC 3'

335D-A	
His-PTPMEG2-471Y-A	F: 5' AGTTCTTGAGCTGGCCAGACGCGGGTGTCCCTTCCTCA 3' R: 5' TGAGGAAGGGACACCCGCGTCTGGCCAGCTCAAGAACT 3'
His-PTPMEG2-471Y-F	F: 5' GCTGGCCAGACTTTGGTGTCCCTTC 3' R: 5' GAAGGGACACCAAAGTCTGGCCAGC 3'
His-PTPMEG2-519I-A	F: 5' ATTGCAGTGCAGGCGCGGGCAGGACAGGT 3' R: 5' ACCTGTCCTGCCCGCGCCTGCACTGCAAT 3'
His-PTPMEG2-559Q-A	F: 5' AGAGGGCCTTCAGCATCGCGACCCCTGAGCAGTACTA 3' R: 5' TAGTACTGCTCAGGGGTCGCGATGCTGAAGGCCCTCT 3'
PCDH-PTPMEG2	F: 5' CCATAGAAGATTCTAGAATGGAGCCCGCGACC 3' R: 5' CGTCGACTGCAGAATTCTTACAGATCCTCTTC 3'
MUNC18-1-GFP-145Y-H	F:5'TTCTCCCCTATGAGTCCCAGGTGCATTCCCTGGACTCCGCTGACTCT 3' R:5'AGAGTCAGCGGAGTCCAGGGAATGCACCTGGGACTCATAGGGGAGAA 3'
MUNC18-1-GFP-145Y-A	F:5'TCTCCCCTATGAGTCCCAGGTGGCTTCCCTGGACTCCGCTGACTCTT 3' R:5'AAGAGTCAGCGGAGTCCAGGGAAGCCACCTGGGACTCATAGGGGAGA 3'
GST-MUNC18-1-145Y-H	F:5'TCCAAAATCGGATCTGGTTCCGCGTGGATCCATGGATTACAAGGATGACGACGATA 3' R:5'CGAGGCAGATCGTCAGTCAGTCACGATGCGGCCGCTCACTCCATTGTTGGAGCCTGATCCTCAAA 3'
GST-MUNC18-1-145Y-E	F:5'TCTCCCCTATGAGTCCCAGGTGGAGTCCCTGGACTCCGCTGACTCTTTCC 3' R:5'GTCAGCGGAGTCCAGGGACTCCACCTGGGACTCATAGGGGAGAAACGC 3'
GST-MUNC18-1-145Y-F	F:5'TCTCCCCTATGAGTCCCAGGTGTTTTCCCTGGACTCCGCTGACTTTTC 3' F:5'GAAAGAGTCAGCGGAGTCCAGGGAAAACACCTGGGACTCATAGGGG 3'
FLAG-VAMP7-45Y-A	F: 5' CTGAAAATAATAAACTAACTGCCTCACATGGCAATTATTTGT 3' R: 5' ACAAATAATTGCCATGTGAGGCAGTTAGTTTATTATTTTCAG 3'
FLAG-VAMP7-45Y-C	F: 5' CTGAAAATAATAAACTAACTTGCTCACATGGCAATTATTTG 3' R: 5' CAAATAATTGCCATGTGAGCAAGTTAGTTTATTATTTTCAG 3'
DYNAMIN1-RFP-354Y-A	F: 5' GAGACCAGATCGACACTGCTGAACTGTCAGGTGGAGCCCG 3' R:5'CTCCACCTGACAGTTCAGCAGTGTCGATCTGGTCTCCAGAACC 3'
DYNAMIN1-RFP-597Y-A	F:5'CACTGAGCAGAGGAATGTCGCTAAGGATTACCGGCAGCTGGAACTG 3'

	R:5'CAGCTGCCGGTAATCCTTAGCGACATTCCTCTGCTCAGTGTTGAA 3'
SNAP25-101Y-A	F:5'TCGCCACCATGGATTACAAGGATGACGACGATAAGATGGCCGAGGACGCAGACATGCGTA 3' R:5'TACGCATGTCTGCGTCCTCGGCCATCTTATCGTCGTCATCCTTGTAATCCATGGTGGCGA 3'

Recombinant lentivirus construction and lentivirus infection.

For recombinant lentivirus packaging, the construction and infection was carried out as previously reported (Zhang et al., 2018). Plasmids carrying different genes including pCDH-PTP-MEG2-GFP, pCDH-PTP-MEG2-$G^{334}R/D^{335}A/Y^{471}A/Y^{471}F/I^{519}A/Q^{559}A$-GFP and pCDH-MUNC18-1-$Y^{145}H/Y^{145}E/Y^{145}F$/WT-GFP were transfected into 293T cells using Lipofectamine TM 2000 (Thermo Fisher, Waltham, MA, USA) according to the manufacturer's instructions. Three days after transfection, the supernatant of virus encoding PTP-MEG2 or MUNC18-1 were collected and filtered. The PTP-MEG2 or MUNC18-1 lentivirus (1×10^6 TU/ml) was used to infect the primary chromaffin cells in later experiments.

ELISA.

Freshly isolated adrenal medullas from adult female mice (6–8 weeks) were cultured in DMEM medium containing 1% penicillin/streptomycin and 10% FBS. After 2 hours starvation, adrenal medullas were stimulated with high KCl (70mM), Angiotensin II (100nM) for 1 min, with or without pre-incubation of a specific PTP-MEG2 inhibitor (2μM) for 2 hours. The supernatants were collected and the epinephrine or norepinephrine secretion were determined by using the Epinephrine or norepinephrine ELISA kit (Shanghai Jianglai Co.,Ltd, JL11194-48T/JL13969-96T) according to the manufacture's protocol.

Electrochemical amperometry

5-mm glass carbon fiber electrode (CFE) was used to measure quantal CA released from the mouse adrenal medulla chromaffin cell as previously described (Liu et al., 2017). We used a Multiclamp 700B amplifier (2012, Axon, Molecular Devices, USA) to perform electrochemical amperometry, which interfaced to Digidata 1440A with the pClamp 10.2 software (Liu et al.,

2017). The holding potential of 780 mV was used to record the amperometric current (Iamp). All experiments were performed at room temperature (20–25°C). The CFE surface was positioned in contact with the membrane of clean primary chromaffin cells to monitor the quantal release of the hormone containing catecholamine substances. In our kinetic analysis of single amperometric spike, we only used the amperometric spikes with S/N > 3 (signal/noise). The standard external solution for our amperometry measurement is as follows: 5 mM KCl, 10 mM glucose, 10 mM HEPES pH 7.4, 2 mM $CaCl_2$, 150 mM NaCl and 2 mM $MgCl_2$. We analysed all data using Igor (WaveMetrix, Lake Oswego, Oregon) and a custom-made macro programme. Statistical data were given as the mean ± SEM and analyzed with t-test or two-way ANOVA.

Electron microscopy

The female mice (6–8 weeks) were decapitated, and the adrenal medullas were freshly isolated and cut to 150-μm-thick sections. The sections were immersed in Ringer's saline (125mM NaCl, 2.5mM KCl, 1.25mM NaH_2PO_4, 26mM $NaHCO_3$, 10mM D-Glucose, 2mM $CaCl_2$, 1mM $MgCl_2$) for 40 minutes at room temperature. During this period, continuous gases of 5% CO_2 and 95% O_2 were offered to the saline to ensure the survival of the tissue slice. After 40 minutes of starvation, the sections were stimulated with different conditions (control; only 100nM AngII agonists for 1 min; only 400nM PTP-MEG2 inhibitor for 45 min; 100nM AngII agonists and 400nM PTP-MEG2 inhibitor for 1 min or 45 min) at 37°C respectively. These sections were firstly immersed in precooled 3% glutaraldehyde and fixed at 4°C for 2 hours, and then rinsed in PBS isotonic buffer, with repeated liquid exchanges and cleaning overnight, so that the samples were thoroughly rinsed and soaked in the buffer. After rinsing, the sample was fixed at 4°C with 1% osmium acid for 2 hours. It was rinsed with isosmotic buffer solution at 0.1M PBS for 15 minutes. The sections were dehydrated with ethanol at concentrations of 50%, 70%, 90%, then ethanol at concentration of 90% and acetone at concentration of 90%, at last only acetone at concentrations of 90%, 100%. We then replaced the acetone with the Epon gradually. The sections were added to Epon and polymerized at 60°C for 36 hours. Ultra-thin sections were performed at the thickness of 60nm by the LKB-1 ultra microtome, and then the ultra-thin sections were collected with the single-hole copper ring attached with formvar film. The sample

was stained with 2% uranium acetate for 30 minutes, and then stained with 0.5% lead citrate for 15 minutes. These prepared samples were examined by JEM-1200EX electron microscope (Japan).

Western

Cells or medulla sections were lysed in lysis buffer (50 mM Tris pH 8.0, 150 mM NaCl, 1 mM NaF, 1% NP-40, 2mM EDTA, Tris-HCl pH 8.0, 10% glycerol, 0.25% sodium deoxycholate, 1mM Na_3VO_4, 0.3μM aprotinin, 130μM bestatin, 1μM leupeptin, 1μM repstatin and 0.5% IAA) after rinsing with the pre-chilled PBS on ice. Cell and tissue lysates were kept on ice for 35 min and then sediment via centrifugation for 15 min at 4 °C. The whole-cell and tissue protein lysates samples (30μg) were prepared for SDS-PAGE. The proteins in the gel were ransferred to a nitrocellulose filter membrane by electro blotting, then probed with the appropriate primary and secondary antibodies. Antibody binding was detected by an HRP system.

Immunofluorescence.

For the acquisition of tissue cells used in immunofluorescence, the mice were decapitated, and the the adrenal medullas were freshly isolated (female mice, 6–8 weeks).The isolated adrenal medullas was immersed in 4% paraformaldehyde for fixation overnight at 4°C. Then the fixed tissues were washed for 4 hours in PBS containing 10% sucrose at 4°C for 8 hours in 20% sucrose, and in 30% sucrose overnight. Then these adrenal medullas were imbedded in Tissue-Tek OCT compound and then mounted and frozen them at -25°C. Subsequently, the adrenal medulla were cut to 4-μm-thick coronal serial sections. The adrenal medullas sections were blocked with 1% (vol/vol) donkey serum, 2.5% (wt/vol) BSA and 0.1% (vol/vol) Triton X-100 in PBS for 1.5 h. Then, the slides were incubated with primary antibodies against PTP-MEG2 (1:100), NSF (1:50), MUNC18-1 (1:50), VAMP7 (1:50), DYNAMIN1 (1:50), SNAP25 (1:100), PACSIN1 (1:50) at 4°C overnight. After washing with PBS for 3 times, the slides were incubated with the secondary antibody (1:500) for 1 h at room temperature. The slides were stained with DAPI (1:2000). Images were captured using a confocal microscope (ZEISS, LSM780). The Pearson's co-localization coefficients were analyzed with Image-Pro Plus.

K_m and k_{cat} measurements.

Enzymatic activity measurement was carried out as previously reported (Wang et al., 2014, Li et al., 2016). The standard solution (DMG buffer) for our enzymatic reactions is following: 50 mM 3,3-dimethyl glutarate pH 7.0, 1 mM EDTA, 1 mM DTT. The ionic strength was maintained at 0.15 M (adjusted by NaCl). For the pNPP activity measurement, 100 µl reaction mixtures were set up in a total volume in a 96-well polystyrene plate (Thermo Fisher Scientific, Waltham, MA, US). The substrate concentration ranging from 0.2 to 5 K_m was used to determine the k_{cat} and K_m values. Reactions were started by the addition of an appropriate amount of His-PTP-MEG2-CD-WT or corresponding mutants, such as $Y^{333}A$, $G^{334}R$, $D^{335}A$, $Y^{471}A$, $Y^{471}F$, $I^{519}A$ and $Q^{559}A$. The dephosphorylation of pNPP was terminated by adding 120µl 1M NaOH, and the enzymatic activity was monitored by measuring the absorbance at 405 nm. The activities toward phospho-peptide segment derived from NSF or MUNC18-1 were measured as following: In the first column, 90µl diluted NSF/MUNC18-1 phospho-peptide substrate (100µM) was added. The successive columns were diluted by 1.5 times. The phospho-peptide substrates were preincubated at 37°C for 5 min. Reactions were started by the addition of an appropriate amount of enzymes. The dephosphorylation of NSF/MUNC18-1 was terminated by adding 120µl Biomol green, and the enzymatic activities were monitored by measuring the absorbance at 620 nm. The steady-state kinetic parameters were determined from a direct fit of the data to the Michaelis-Menten equation using GraphPad Prism 5.0.

GST-pull down.

To screen the candidate proteins interacting with PTP-MEG2, the GST beads were washed five times by cold binding buffer (20mM HEPES pH7.5, 1mM DTT, 1mM EDTA, and 100mM NaCl) and incubated with 5µg purified GST-PTP-MEG2-CD-$D^{470}A$ protein for 2 hours at 4°C. PC12 cells were transfected with FLAG-SYN1-GFP, FLAG-MUNC18-1-GFP, FLAG-STXBP3-GFP, FLAG-PACSIN1-GFP, FLAG-SCAMP1-GFP, FLAG-PPP3CA-GFP, FLAG-STX17-GFP, FLAG-VAMP7, FLAG-SYT7-GFP, FLAG-SYT11-GFP, FLAG-SNAP25-GFP, FLAG-DYNAMIN-1-GFP. After stimulation with 100µM Na_3VO_4 and 100µM H_2O_2 for 10 minutes at 37 °C, the cells were washed and then lysed in lysis buffer [20 mM HEPES pH 7.5, 100 mM NaCl, 0.5% NP-40, 5 mM iodoacetic acid, and a protease inhibitor mixture (final

concentrations, 10μg of leupeptin, 1μg of aprotinin, 1μg of pepstatin, 1μg of antipain, and 20μg of phenylmethylsulfonyl fluoride per ml), 10mM DTT, 2mM EDTA] on ice for 30 minutes, then centrifuged at 12000rpm for 15 minutes at 4 °C. 20μl GST beads- PTP-MEG2-$D^{470}A$ protein was added into 500μl supernatants and the mixtures were subjected to end-to-end rotation at 4 °C for 2 hours. The GST beads and their binding proteins were washed five times with cold binding buffer to exclude the unspecific binding proteins.

The pull down experiment of MUNC18-1 and SYNTAXIN1 were described similar to above description. The GST beads were washed five times by cold binding buffer (described as above). After that, 5μg purified GST-MUNC18-1-WT or its $Y^{145}H$, $Y^{145}E$ or $Y^{145}F$ mutant proteins were added into 20μl GST-agarose, and incubated at for 4 °C 2 hours with end to end rotation. PC12 cells transfected with FLAG-SYNTAXIN1 were lysed in lysis buffer (described as above) and centrifuged to remove the pallets. The supernatants were added with 20μl GST beads/GST-fusion protein and the mixtures were subjected to end-to-end rotation at 4 °C for 2 hours. The FLAG-SYNTAXIN1 was detected with FLAG antibody.

Immunoprecipitation and in vitro dephosphorylation

Rat adrenal medullas were isolated and cut into pieces in D-hanks buffer, and stimulated with 70mM KCl or 100nM AII for 2 minutes. The tissues were then lysed and grinded on ice in lysis buffer supplemented with proteinase inhibitor as described before. The lysates were centrifuged at 12000 rpm for 20 minutes at 4 °C and the pallets were removed. Before incubation with the lysates in the later step, the 10μg primary antibodies of NSF, MUNC18-1, VAMP7 or SNAP25 were incubated with 60μl Protein A/G beads by end-to-end rotation overnight at 4 °C. Then the supernatants were incubated with primary antibody pre-coated with Protein A/G beads and rotated for 2 hours. 60μg purified PTP-MEG2-WT protein or control solution were added into the lysates for the in vitro dephosphorylation. A pan-phospho-tyrosine antibody pY^{20} was used in Western blotting to detect the phosphorylated tyrosine of NSF/MUNC18-1/VAMP7/SNAP25 in adrenal medullar with or without incubation with the PTP-MEG2.

Protein Expression and Purification

The wide type and mutant proteins of His-tagged PTP-MEG2-catalytic domain were expressed

in BL21-DE3 Escherichia coli as previously described (Pan et al., 2013). In brief, 0.4 mM isopropyl1-thio-D-galactopyranoside (IPTG) was used to induce the expression of His-PTP-MEG2, and the bacteria lysates were centrifuged at 12000 rpm for 1 hour. Ni-NTA Agrose was applied to bind the His-tagged PTP-MEG2 and an imidazole gradation was used to elute the binding proteins. His-PTP-MEG2 was then purified with gel filtration chromatography to achieve at least 95% purity. The wide type and mutant proteins of GST-PTP-MEG2 and GST-MUNC18-1 were also expression in E.coli in presence of 0.4 mM IPTG for 16 hours at 25°C. After centrifugation and lysis, the proteins were purified by binding with GST-Sepharose for 2 hours and eluted by GSH.

Crystallization and Data Collection

For crystallization, His-PTP-MEG2-$C^{515}S/D^{470}A$ protein (concentration at 15mg/ml) was mixed with NSF-pY^{83} peptide (EVSLpYTFDK) or MUNC18-1-pY^{145} peptide (ESQVpYSLDS) with molar ratio as 1:3 in buffer A (pH 7.2, 20 mM Hepes, 350 mM NaCl, and 1 mM DTT). 1μl mixed protein was blended with 1μl buffer B (pH 6.4, 20% PEG 4000, 0.2M KSCN, 10% ethelene glycol, 0.1M bis-tris propane) at 4°C for 3 days before crystals appears. The cubic crystals were preserved in liquid nitrogen very quickly dipped in storage buffer (buffer B supplemented with 10% glycerol). The data were collected at Shanghai Synchrotron Radiation Facility beamline BL17U1 using 0.98Å X-ray wave length and analyzed by HKL2000.

Structural determination and refinement

The crystals of PTP-MEG2-NSF-pY^{83} and PTP-MEG2-MUNC18-1-pY^{145} peptides belong to the $P2_12_12$ space group. In each asymmetric unit, both PTPMEG2-NSF-pY^{83} and PTPMEG2-MUNC18-1-pY^{145} contain one monomer in one unit. Molecular replacement with Phaser in the CCP4 software package, with PTP-MEG2 catalytic domain (PDB code: 2PA5, water deleted) as the initial search model. Further refinements were carried out using the PHENIX program with iterative manual building in COOT. The data of the final refined structures are shown in Supplementary information Table S1.

Bioinformatic search of PTP-protein interactions

We identified the PTP-protein interactions by two independent bioinformatic analyses. On one site, we extracted the potential PTP-interacting proteins from the STRING database (Szklarczyk et al., 2015) by setting the parameters of Homo sapiens. On the other site, we used Pubtator (Wei et al., 2013) to text-mine potential PTP-protein associations from PubMed literature (by 2018.9) via the search of combinational keywords such as "tyrosine phosphorylation mutation, vesicular, fusion, and human". We compared these two protein lists to produce a consensus PTP-interacting protein list. Subsequently, we narrowed down the protein list by satisfying following constraints: (a) The protein should express in the adrenal gland as documented in the TissueAtlas (Thul et al., 2017); (b) The protein should expose tyrosine residue(s) on surface for phosphorylation as simulated by the Molecular Operating Environment (MOE) (Vilar et al., 2008); (c) On the protein, at least one predicted tyrosine phosphorylation site predicted by the PhosphoSitePlus (Hornbeck et al., 2015) is also experiment-validated. The refined PTP-protein pairs were then ready for later experimental analyses.

Statistical analysis

All data are presented as mean ± SEM. The statistical significance between different groups was compared with ANOVA tests, and the statistical significance between two different groups was generated by student's t test. All of the Western films were scanned, and band intensity was quantified with ImageJ software (National Institutes of Health, Bethesda MD). $P < 0.05$ was considered as statistically significant.

Table -1 Crystallographic Data and Refinement Statistics